

AD _____

Award Number: W81XWH-07-1-0428

TITLE: Nanotechnology-Enabled Optical Molecular Imaging of Breast Cancer

PRINCIPAL INVESTIGATOR: Dr. Rebekah Drezek

CONTRACTING ORGANIZATION: William Marsh Rice University
Houston, TX 77005

REPORT DATE: July 2011

TYPE OF REPORT: Annual

PREPARED FOR: U.S. Army Medical Research and Materiel Command
Fort Detrick, Maryland 21702-5012

DISTRIBUTION STATEMENT: Approved for public release; distribution unlimited

The views, opinions and/or findings contained in this report are those of the author(s) and should not be construed as an official Department of the Army position, policy or decision unless so designated by other documentation.

REPORT DOCUMENTATION PAGE				Form Approved OMB No. 0704-0188	
Public reporting burden for this collection of information is estimated to average 1 hour per response, including the time for reviewing instructions, searching existing data sources, gathering and maintaining the data needed, and completing and reviewing this collection of information. Send comments regarding this burden estimate or any other aspect of this collection of information, including suggestions for reducing this burden to Department of Defense, Washington Headquarters Services, Directorate for Information Operations and Reports (0704-0188), 1215 Jefferson Davis Highway, Suite 1204, Arlington, VA 22202-4302. Respondents should be aware that notwithstanding any other provision of law, no person shall be subject to any penalty for failing to comply with a collection of information if it does not display a currently valid OMB control number. PLEASE DO NOT RETURN YOUR FORM TO THE ABOVE ADDRESS.					
1. REPORT DATE (DD-MM-YYYY) 01-07-2011		2. REPORT TYPE Annual		3. DATES COVERED (From - To) 15 JUN 2010 - 14 JUN 2011	
4. TITLE AND SUBTITLE Nanotechnology-Enabled Optical Molecular Imaging of Breast Cancer				5a. CONTRACT NUMBER	
				5b. GRANT NUMBER W81XWH-07-1-0428	
				5c. PROGRAM ELEMENT NUMBER	
6. AUTHOR(S) Dr. Rebekah Drezek E-Mail: drezek@rice.edu				5d. PROJECT NUMBER	
				5e. TASK NUMBER	
				5f. WORK UNIT NUMBER	
7. PERFORMING ORGANIZATION NAME(S) AND ADDRESS(ES) William Marsh Rice University Houston, TX 77005				8. PERFORMING ORGANIZATION REPORT NUMBER	
9. SPONSORING / MONITORING AGENCY NAME(S) AND ADDRESS(ES) U.S. Army Medical Research and Materiel Command Fort Detrick, Maryland 21702-5012				10. SPONSOR/MONITOR'S ACRONYM(S)	
				11. SPONSOR/MONITOR'S REPORT NUMBER(S)	
12. DISTRIBUTION / AVAILABILITY STATEMENT Approved for Public Release; Distribution Unlimited					
13. SUPPLEMENTARY NOTES					
14. ABSTRACT This project focuses on development of nanotechnology-enabled optical molecular imaging technologies for applications in both breast cancer diagnosis and monitoring therapeutic response. The project consists of two major efforts: (1) optical instrumentation technology development and (2) development of complementary engineered nanomaterials for use in conjunction with the instrumentation created to provide molecular specificity. A particularly significant effort is underway to develop needle-compatible fiber optic probes to enable in vivo imaging of tumors with micron resolution in order to provide a new microscopic, high resolution imaging modality. These microscopic devices will complement the macroscopic, wide-field optical imaging devices being developed in this project.					
15. SUBJECT TERMS nanotechnology, molecular imaging, optical imaging					
16. SECURITY CLASSIFICATION OF:			17. LIMITATION OF ABSTRACT UU	18. NUMBER OF PAGES 59	19a. NAME OF RESPONSIBLE PERSON USAMRMC
a. REPORT U	b. ABSTRACT U	c. THIS PAGE U			19b. TELEPHONE NUMBER (include area code)

Table of Contents

Introduction.....	2
Body.....	3
Key Research Accomplishments.....	31
Reportable Outcomes.....	32
Conclusion.....	34
References.....	35
Appendices.....	39

Introduction

There is a critical need to develop new imaging technologies which bridge the gap between our rapidly developing fundamental molecular understanding of breast carcinogenesis and our ability to rationally harness this understanding to develop more effective diagnostic and treatment strategies. Bridging that gap requires developing new tools which can rapidly detect, diagnose, and at times, intervene in the disease process based on recognition of specific molecular signatures of breast cancer *in vivo*. In this project, we focus on the development of photonics-based imaging technologies (SOW, Project 1 and Project 2) and complementary nanoscale molecular-targeted imaging agents for detection and monitoring applications (SOW, Project 3) in order to provide a new approach to molecular imaging of breast cancer. Medical imaging plays a prominent role in all aspects of the screening, detection, and management of breast cancer today. A variety of imaging methods including screening and diagnostic x-ray mammography and resonance imaging (MRI) are currently used to evaluate and monitor breast lesions. Although existing imaging technologies provide a useful approach to delineating the extent of tumors, these methods offer only low resolution, non-specific issues of tissue and cannot provide a detailed picture of the molecular profile of a tumor. In addition, techniques such as x-ray imaging and MRI are not able to detect small early cancers or pre-cancerous breast lesions and are difficult to use in settings such as the operating room where near real-time dynamic images are required. Thus, there is a substantial clinical need for novel imaging methods for the detection and monitoring of breast cancers which offer improved sensitivity, specificity, portability, and cost-effectiveness. In this project we develop portable optical technologies which promise high resolution, noninvasive functional imaging of tissue at competitive costs. Optical approaches can detect a broad range of morphological, biochemical, and architectural tissue features directly relevant to characterizing breast lesions including sub-cellular physical parameters such as nuclear size and nuclear to cytoplasm (N/C) ratios and biochemical indicators such as hemoglobin concentration, metabolic rate, and collagen cross-linking levels. To make these technologies even more powerful we are expanding the current capabilities of photonics-based imaging approaches with the additional capacity to quantitatively and dynamically detect molecular markers of breast cancer *in vivo* without tissue removal or directly after removal in a surgical environment (SOW, Project 3). Developing the optical molecular imaging tools and agents for breast cancer which will allow us to accomplish this goal is the focus of this project. We have now completed four years of effort on this project. The SOW has been modified once to reflect revised goals. In addition, an exempt protocol was approved by Rice University's IRB and DoD for acquisition of human breast cancer tissue specimens so that work could extend beyond the cell level studies originally proposed.

Progress Report Body

As in past years, in this report we focus our detailed descriptions of our progress on work which has not yet been submitted for publication. In addition, we enclose copies of published papers not previously submitted in prior reports (including one paper previously submitted in manuscript form) but do not discuss that work in detail within the report body. We have organized our Year 4 report slightly differently than prior reports. Rather than presenting technical updates project by project, this report instead begins where our Year 3 report ended. In the last section of our Year 3 report, we discussed our initial efforts towards ultimately bringing together efforts in Projects 1 and 2 (optical imaging instrumentation) and Project 3 (nanotechnology-based imaging agents) to address a practical clinical problem: assessing tumor margins in breast cancer patients. In Section I below, we first provide continued progress on that aspect of the work, which has progressed from initial studies using thin histological section to whole breast specimens. After this discussion, in Section II we provide individual technical highlights for Projects 1, 2, and 3 as described in our revised Statement of Work. For the newest work currently in progress, we also describe studies not yet conducted we aim to complete in Year 5.

(I) Combining Scattering-Based Optical Imaging Technologies and Targeted Nanoengineered Imaging Agents for Tumor Margin Detection in HER2+ Women

Introduction

Currently, breast cancer is the second leading cause of cancer-related deaths in women and it accounts for approximately one-third of all cancers diagnosed in women in the United States (Cancer, 2005). In order to reduce cancer recurrence and progression, cancerous tissue must be completely eliminated, regardless of grade (Steen, 1993). Surgical breast cancer therapy focuses on removing the primary tumor and identifying the possibility of disease spread through evaluation of sentinel lymph nodes. Although some patients may require modified radical mastectomy, which involves the complete removal of the entire breast, many patients with less-advanced breast cancer elect breast-conserving surgery. To reduce the likelihood of cancer recurrence, it is recommended that patients undergoing a breast conservation therapy, such as lumpectomy, receive adjuvant radiation treatment to combat potential residual cancerous cells and maintain local control (Buckman, 1997; Fisher et al., 2002). Fisher *et al.* determined that

lumpectomy followed by radiation therapy is just as effective as mastectomy provided that the resected tissue specimens contain negative tumor margins (Fisher et al., 2002). Intraoperative treatment decisions are, therefore, absolutely critical. The presence of a positive surgical margin has been associated with lower rates of patient survival (Mojica CM, 2007). Due to residual cancer cells being left in many patients that undergo breast conservation therapy, as many as 40% of patients have experienced local breast cancer recurrence near the site of the original tumor (Fisher et al., 2002).

Presently, intraoperative tumor margin detection occurs only in specialized tertiary centers, such as The University of Texas M.D. Anderson Cancer Center (MDACC). In these centers, the resected tissue receives a preliminary evaluation by a pathologist while the patient remains in the operating room, and more tissue can be removed until the pathologist determines the tumor margins are negative. In community hospitals, however, pathologic analysis of excised tissue does not occur until well after the operation is complete. Those patients who consequently have positive tumor margins must return for an additional surgical procedure or receive increased doses of post-operative radiation therapy (Smitt et al., 1995; Oouchi et al., 2009). Thus, the existence of positive tumor margins subsequently portends additional risks and costs to the patient. Due to the existing limitations of current intraoperative tumor margin detection, there is an opportunity to develop superior diagnostic tools to assist in reducing the recurrence and progression of cancer due to inadequate tissue removal during primary surgery.

While histologic (and thus, microscopic) analysis remains the gold standard for tumor margin assessment, the macroscopic evaluation of tissue specimens may also be used to provide an intraoperative estimate of tumor margin status prior to subsequent processing. Currently, macroscopic evaluation occurs for breast cancer specimens that involve microcalcifications or nonpalpable masses and does not occur for palpable breast masses (Cabioglu et al., 2007). For nonpalpable masses that have been resected, the specimen is first oriented with sutures prior to delivery to pathology. The whole specimen is then radiographed and inked by pathologists to further orient the specimen as to *in situ* location. The radiographic images are used to determine the extent of the breast disease and the proximity to the resected margins. Although specimen radiography appears to increase the accuracy of tumor margin detection, limitations have been noted. For instance, microcalcifications are not always associated with malignancy and areas that appear as tumor on radiographic images may actually be areas of lymphocytic accumulation

due to nonneoplastic conditions (Graham et al., 1994). In order to increase the sensitivity and specificity associated with macroscopic evaluations, the use of contrast agents targeted to specific biomarkers associated with disease may present superior opportunities.

In studies we reported in our Year 2 and Year 3 report, we confirmed that silica-based gold nanoshells targeted to the human epidermal growth factor receptor 2 (HER2) could be used for the rapid contrast enhancement of both cells (Bickford et al., 2008a) and tissue sections (Bickford et al., 2010) which overexpress HER2 biomarkers (Year 2 and Year 3, respectively). Amplification of this cell-surface bound tyrosine kinase receptor, which occurs in approximately 20-25% of all human breast cancers, is associated with increased cancer aggression, recurrence, and progression (Slamon et al., 1987; Nahta et al., 2006). Accurate tumor margin detection is thus particularly critical for patients who overexpress HER2 in order to minimize the devastating sequelae associated with this disease. To facilitate prompt tumor margin detection intraoperatively, the ability to assess tumor margins without the need for physical sectioning is highly desirable. Thus, in this study, we advance our previous findings by examining the ability to rapidly target HER2 receptors in intact *ex vivo* human breast tissue specimens without sectioning. We first confirm the predominance of the surface targeting needed to identify the tumor margins and preferential labeling of HER2-positive tissue. Then, we demonstrate the proof of concept that anti-HER2 targeted gold nanoshells can be used as rapid diagnostic imaging agents for HER2-overexpression in intact breast tissue specimens using a standard stereomicroscope and confirm these results through reflectance confocal microscopy and immunohistochemistry. In Year 5, this work will continue through similar studies this time using the optical imaging devices developed in this DoD project.

Nanoshell Fabrication and Antibody Conjugation

Nanoshells were fabricated as formerly described (Loo et al., 2004; Loo et al., 2005a; Loo et al., 2005b) and only a brief summary will be provided here. Silica cores were made using the Stöber method (Stober et al., 1968) followed by subsequent termination of the silica surfaces with amine groups. The final particles were measured by dynamic light scattering (DLS) to have an average diameter of 276 nm. Next, gold colloid (diameter of ~1-3 nm) was fabricated and adsorbed onto the surface of the silica cores via the amine groups (Duff et al., 1993). After the gold shell layer

over the silica cores was completed, the spectrum of the final nanoshell solution was visualized using a UV-vis spectrophotometer (Varian Cary 300) (Fig.1).

In order to determine the concentration of nanoshells in solution, the absorption, scattering, and extinction coefficients were determined using Mie Theory. The average size of the nanoshells, as validated by Scanning Electron Microscopy (SEM), was a diameter of 314 nm with a peak surface plasmon resonance at 840 nm (see Fig. 1). The concentration of the working nanoshell solution was approximately 2.0×10^9 particles/mL.

Nanoshells were next targeted to biological HER2-antigens by linking the surfaces of the nanoshells to anti-HER2/neu antibodies using previously described methods (Loo et al., 2004). Prior to beginning experimental studies, nanoshells (2.0×10^9 particles/mL) were incubated with an anti-HER2-linker cocktail (Loo et al., 2004) for 2 hours at 4°C. For the purpose of complete nanoparticle stabilization in biological media, the nanoshells were next incubated with a 1 mM polyethylene glycol-thiol solution (PEG-SH, MW = 5kD, Nektar) for 12-16 hours at 4°C. Next, unbound antibodies and excess PEG-SH were removed from the nanoshells by centrifugation. Supernatant was removed and, just prior to experimental tissue studies, the nanoshells were resuspended in antibody diluent (IHC World, pH 7.4) by gentle pipetting to a final volume of 165 μ L.

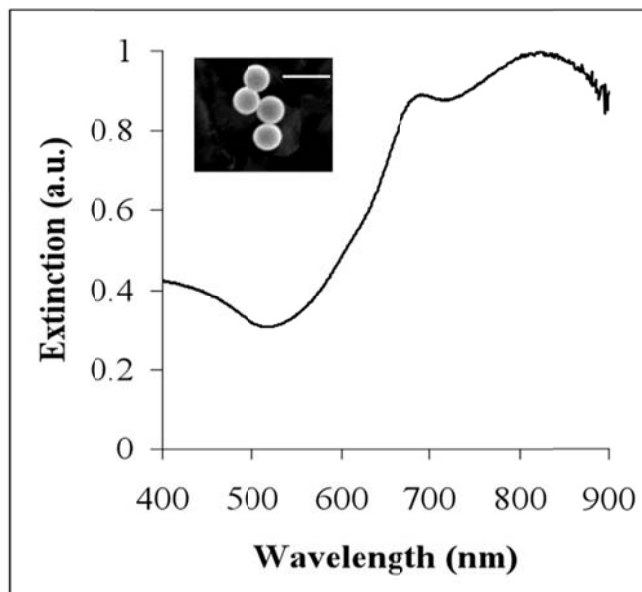


Figure 1. Measured extinction spectra of nanoshells with an average core diameter of 276 nm and average shell thickness of 19 nm. Insert depicts corresponding image from scanning electron microscopy. Scale bar represents 500 nm

Ex Vivo Human Breast Tissue Specimens

Normal (nonneoplastic) and cancerous (HER2-negative and HER2-positive) breast tissue specimens were supplied by the Cooperative Human Tissue Network (CHTN) through a protocol

approved by the Institutional Review Board (IRB). Tissues were previously designated as normal or cancerous by pathologists at the medical centers where the tissue samples were obtained. Additionally, HER2/neu status was also previously determined by pathologists at the respective medical centers prior to the patients undergoing any form of medical treatment. The tissues, which arrived as pre-frozen in liquid nitrogen, were immediately placed in a -80°C freezer.

Prior to use, samples were thawed briefly in a 37°C water bath and then cut on a disposable cutting board using a 5 mm punch biopsy in order to maintain size consistency. At least two punch biopsies were taken from each specimen for control and experimental conditions. Each cut specimen used was 5 mm in diameter with an average thickness of 1 mm. Tissue samples were subsequently incubated in prewarmed antibody diluent (IHC World, pH 7.4) for 1 minute at room temperature with gentle agitation in a 24-well plate. After pre-rinsing, the samples were incubated in either antibody diluent or the aforementioned targeted-nanoshell cocktail (volume = 165 μ l) in polyethylene sample vials (Sigma Aldrich). The vials were then placed on a nutator in an incubator set at 37°C for 5 minutes. After incubation, the tissue samples were removed from the vials and rinsed 3 times in 1X PBS briefly in a 24-well plate. Samples were then moved to a clean well of 1X PBS prior to imaging.

Two Photon Imaging of Human Breast Tissue Specimens

For two photon imaging of intact breast tissue specimens, both HER2-negative cancerous and HER2-positive cancerous samples were evaluated for surface labeling of HER2-targeted nanoshells. Samples were placed directly on a glass coverslip (Fisher Scientific) and an additional coverslip was placed on top of the tissue in order to facilitate moderate tissue compression. For image acquisition, a Zeiss laser scanning microscope (LSM) 510 non-linear optics (NLO) META multi-photon system was used in tandem with a Coherent Chameleon femtosecond-pulsed, mode-locked Ti:sapphire laser. This system was set to operate as formerly described (Bickford et al., 2008b). Specifically, an excitation wavelength of 780 nm and a power of 10% of the maximum excitation power were used. The collected emission wavelength range spanned from 451 nm to 697 nm. Images were collected at a magnification of 20X and a z-stack (depth) increment of 5 μ m. In order to calculate the percentage of area covered by nanoshells, Image J imaging software was implemented after image acquisition. An intensity

threshold of 30 (on a scale of 0 to 255, where 0 represents pure black and 255 represents pure white) was used to distinguish areas with and without nanoshells. For areas that did not contain nanoshells, the associated intensities did not exceed the threshold.

Macroscopic Imaging of Human Breast Tissue Specimens

Normal (nonneoplastic) and HER2-positive cancerous breast tissue specimens (from patients who had and had not received previous neoadjuvant chemotherapy) were imaged using a Zeiss Discovery.V8 stereomicroscope equipped with a VisiLED MC1000 light source. This microscope provides enhanced visualization of specimens in three dimensions ranging from 1X to 8X magnification. For macroscopic imaging of breast tissue specimens, a thin plastic black stage was placed beneath a 22 μm x 22 μm glass coverslip (Fisher Scientific) to enable ease of tissue placement and to provide a consistent black background among all samples. The specimens (controls and respective nanoshell-labeled counterparts) were placed alongside each other on top of the coverslip. Images were taken at both 1X and 2X magnification under the same lighting conditions.

Reflectance Confocal Microscopy Imaging of Human Breast Tissue Specimens

Following widefield imaging, the aforementioned samples were prepared for microscopic imaging under reflectance confocal microscopy. For this component of the study, a Lucid VivaScope 2500 inverted confocal microscope was employed, which uses an 830 nm light source and has a lateral resolution of less than 2 μm . Samples were placed directly on glass slides (Fisher Scientific) which were modified by the addition of an adhesive 1-mm-deep, 20-mm-diameter silicon isolator (Invitrogen). In order to compress the tissue slightly and consistently among samples, an adhesive tissue cassette (Lucid, Inc.) was placed directly on top of the silicone isolators above the tissue specimens. Multiple images were taken at a power of 0.4 mW and at the same distance from the glass surface for tissue samples incubated in either antibody diluent alone or the HER2-targeted nanoshells. After reflectance imaging, coverslips and silicone isolators were removed and the samples were prepared for histological processing. Additionally, reflectance intensity measurements were recorded using Image J processing software as described previously (Bickford et al., 2010).

Immunohistochemistry and Histology

Once images were collected under both stereomicroscopy and RCM imaging systems, normal (nonneoplastic) and HER2-positive cancerous samples (with and without previous neoadjuvant chemotherapy) were embedded in OCT media (BBC Biochemical) and frozen rapidly over dry ice. Sections were then made of all specimens using a Leica CM1850 UV cryostat. At least 20 sections were cut from each specimen at a thickness of 5 μm . Cancerous specimens were sectioned at -20°C and normal specimens were sectioned at -30°C , as recommended by Leica for maintaining optimal tissue morphology. The sections were immediately placed on superfrost slides (Fisher Scientific) and allowed to air dry overnight. The next day, multiple sections from each specimen of interest were prepared for either immunohistochemistry (IHC) or hemotoxylin and eosin (H&E) staining. IHC for the HER2-antigen was executed using the Histostain Plus AEC Broad Spectrum Kit (Invitrogen) per manufacturer's instructions. H&E staining was also performed using the manufacturer's instructions (Sigma Aldrich) for the alcoholic Eosin Y solution. For image acquisition, a standard brightfield microscope (Zeiss Axioskop 2 equipped with a Zeiss Axiocam MRc5 color camera) was used at a magnification of 20X under the same lighting conditions.

Results

Distribution and Penetration of Gold Nanoshells in Intact Human Breast Tissue

The goal of this study was to evaluate the distribution of anti-HER2-conjugated gold nanoshells on resected intact tissue specimens. For comparison, the nanoshell labeling between HER2-positive and HER2-negative tissue samples was evaluated. In order to do this, a two photon imaging system was employed. As shown previously, this imaging system is capable of enhancing and capturing the luminescence signature of the gold nanoshells (Bickford et al.) while also creating a stack of images taken in the z-direction throughout the depth of the tissue of interest. It should be noted that the acquisition of images in the z-direction with this system employs the Nyquist Sampling Theorem, where images overlap by half their thickness in order to avoid missing information.

Figure 2 represents the z-stack images of HER2-positive and HER2-negative tissues incubated with HER2-targeted nanoshells. Each sequential increment in the z-direction represents 5 μm into the tissue. Qualitatively, the first image (taken at the surface, or at 0 μm) in Fig. 2 demonstrates that the nanoshells preferentially label HER2-receptors on the surface of the tissue. Additionally, Fig. 2 displays decreased signal as the focal spot from the confocal microscope penetrates further into the tissue. This is possibly due to the reduced number of nanoshells that were able to penetrate the tissue in the limited amount of incubation time, thus decreasing signal collected at each penetration depth. However, due to the optical set-up, one cannot conclusively determine if the signal seen at these depths is due to nanoshell presence, or

reflection from the nanoshells attached to the surface. Future experiments, such as slicing the tissue after incubation with the nanoshells will conclusively determine the penetration depth of the nanoshells.

Additionally, a quantitative difference of the nanoshell signal at the surface of the Her2-positive and Her2-negative tissue was calculated. Using ImageJ imaging software, it was calculated that approximately 66% of the Her2-positive field of view area was covered in nanoshells versus just 2% for the Her2-negative field of view. This confirms that anti-Her2 nanoshells can be used to discriminate Her2-positive cancerous tissue from Her2-negative noncancerous tissue

Enhanced Optical Imaging of Intact Ex Vivo Human Breast Cancer Tissue Using Gold Nanoshells

Based on the two-photon results demonstrating the superior labeling of HER2-targeted nanoshells on the surface of intact *ex vivo* HER2-positive tissue specimens, we assessed the potential of using a standard stereomicroscope to visualize this enhanced contrast. For this component of the study, human breast tissue specimens that over-expressed HER2 receptors at the time of patient diagnosis were evaluated and compared to normal (nonneoplastic) tissue. Due to the ultimate goal of utilizing gold nanoshells to rapidly label tumor margins intraoperatively in diverse patient populations, we examined tissue from patients who had and had not undergone neoadjuvant chemotherapy. All tissue samples were incubated with either antibody diluent buffer or the anti-HER2-targeted nanoshells for 5 minutes at 37°C. As shown in Fig. 3, which represents raw images taken with a stereomicroscope, intact tissue specimens incubated with antibody diluent alone showed no markings or features characteristic of nanoshells. However, tissue specimens incubated with the anti-HER2-targeted nanoshells demonstrate numerous particles on the surfaces of the tissues. Qualitatively, the HER2-positive tissue from the patient who did not undergo previous chemotherapy shows the greatest labeling with the targeted nanoshells. The HER2-positive tissue from the patient who did undergo neoadjuvant chemotherapy does demonstrate enriched nanoshell labeling when compared to HER2-negative normal tissue, though not to the same extent as the patient without previous chemotherapy. In contrast, the nonneoplastic tissue shows the least amount of nanoshell labeling and only a few areas of nanoshells can be visually perceived.

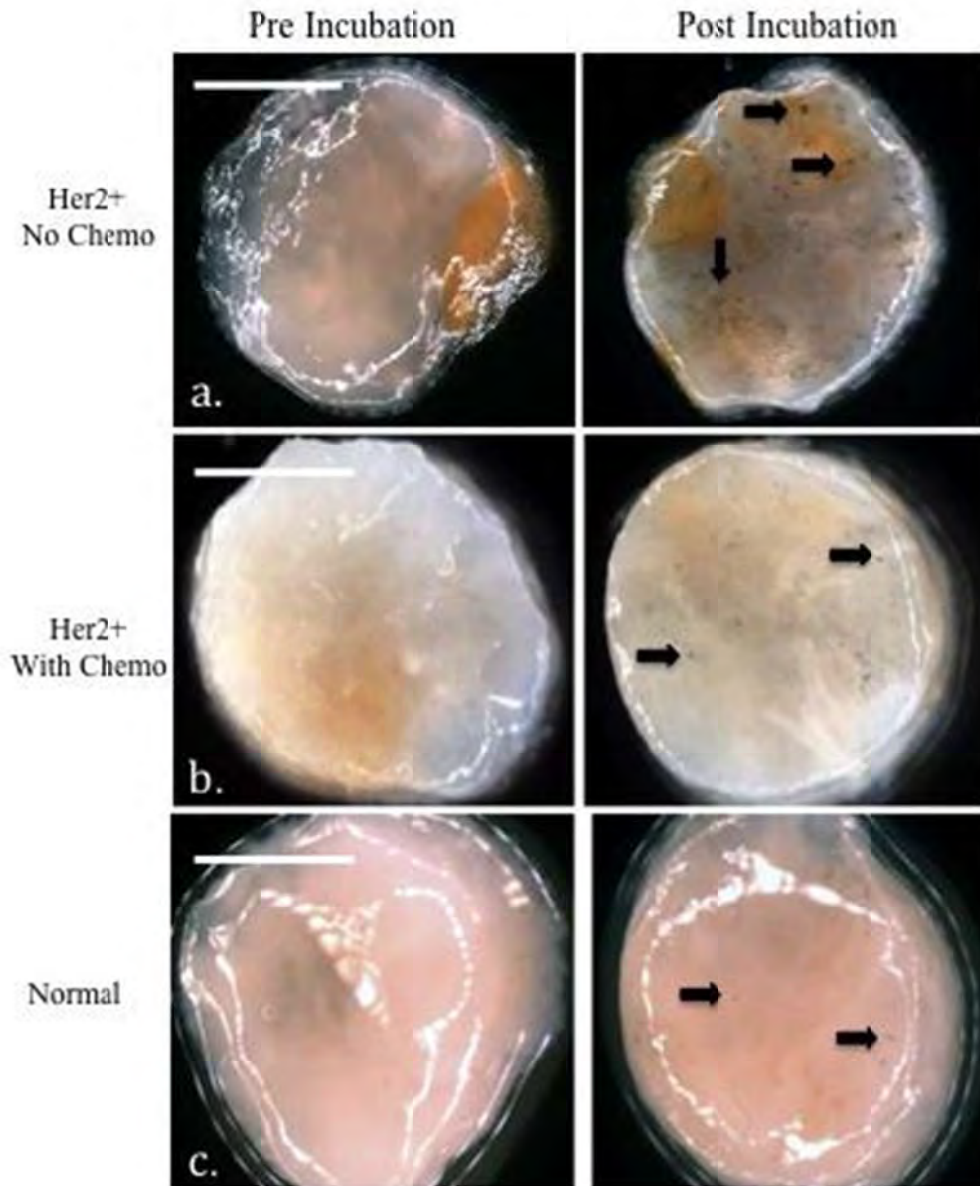


Figure 3. Raw stereomicroscope images of (a.,b.) HER2-overexpressing cancerous and (c.) nonneoplastic tissue incubated with either buffer or HER2-targeted nanoshells for 5 minutes at 37°C. Cancerous tissue taken from a patient (a.) without chemotherapy and (b.) following neoadjuvant chemotherapy. Arrows represent nanoshells. Images taken at 2X. Scale bars = 2.5 mm.

While the degree of nanoshell labeling can be visualized without image adjustments under a standard stereomicroscope, the superior extent of this labeling can be seen more clearly after a simple contrast enhancement using imaging software (Image J). As seen in Fig.4 (a.), the

nanoshells are even more discernable against the tissue background regardless of inherent tissue constituents.

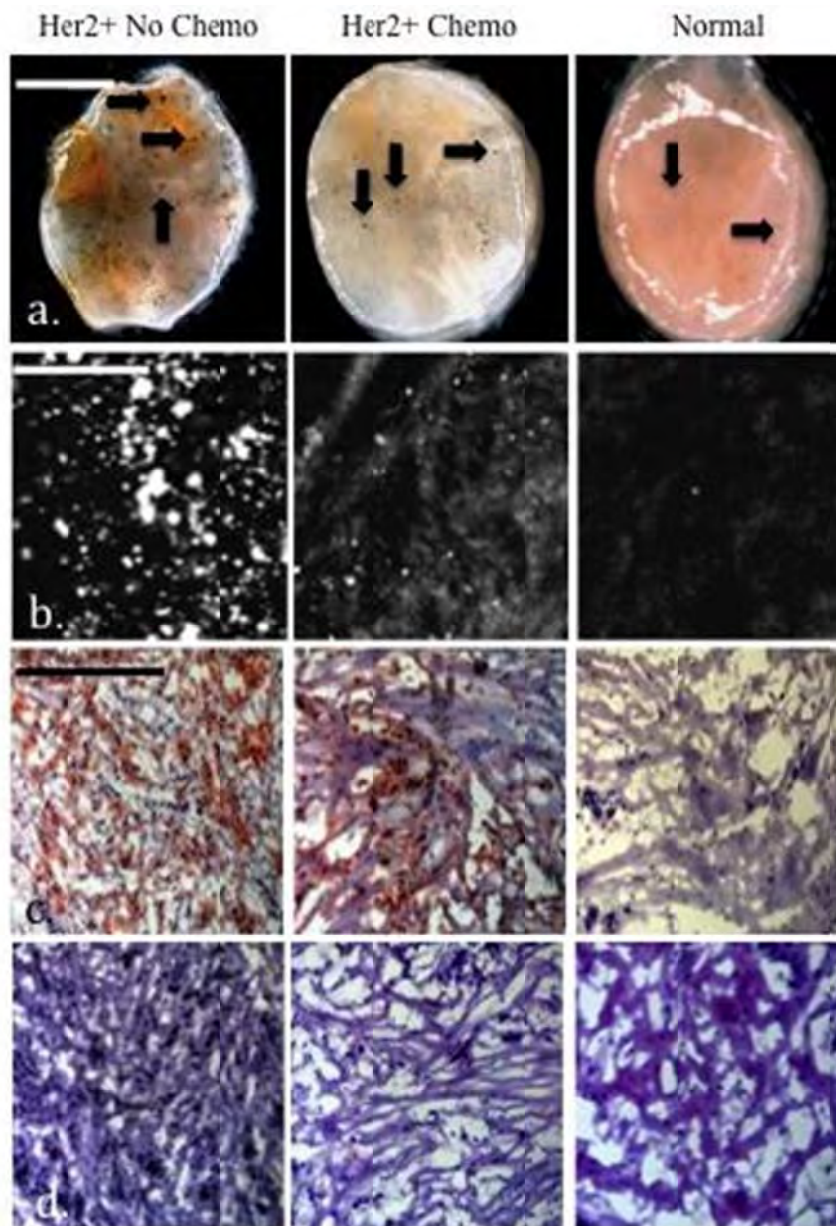


Figure 4. (a.) Stereomicroscopic images of HER2-overexpressing breast tissue (with and without neoadjuvant chemotherapy) and normal breast tissue incubated with HER2-targeted nanoshells for 5 minutes at 37°C after contrast enhancement. Magnification at 2X; scale bar = 2.5 mm. Arrows represent nanoshells. (b.) Respective reflectance confocal microscopy images of tissue samples from (a.). Power = 0.4 mW and scale bar = 75 μ m. Respective (c.) HER2/neu immunohistochemistry and (d.) H&E results taken under brightfield microscopy under 20X magnification. Scale bar = 0.35 mm

In order to validate the enhanced nanoshell labeling seen by macroscopic imaging, the surfaces of the same tissue samples were also imaged using reflectance confocal microscopy

(Fig.4 (b.)). Concurring with the stereomicroscopic images, we see dramatic nanoshell surface-labeling when using targeted nanoshells with previously untreated HER2-positive tissue. For the HER2-positive sample, which had formerly undergone chemotherapy, we also see enhanced nanoshell labeling, though to a lesser degree than the untreated sample as suggested by the stereomicroscopy results. The normal, nonneoplastic tissue displays the least amount of surface labeling with only minimal nanoshells evident with either imaging system. Reflectance intensity measurements (data not shown) were ~2.5 to 3 times greater for both the HER2-positive tissue sample receiving chemotherapy and for the HER2-positive tissue not receiving chemotherapy when compared to the normal HER2-negative tissue sample.

Subsequent histological analysis shown in Fig. 4 (c.) reveals that the distribution of HER2 receptors seen with nanoshell-enabled contrast corresponds to that seen with IHC against HER2. The HER2 expression seen by IHC is greater for the previously untreated HER2-positive tissue sample than for the sample which had undergone neoadjuvant chemotherapy. This is believed to be due to the effects of chemotherapy. Rasbridge *et al.* previously demonstrated that patient response to chemotherapy is highly variable, with patients previously negative for HER2-overexpression occasionally becoming positive after treatment and patients previously positive for HER2-overexpression subsequently becoming negative (Rasbridge et al., 1994). In as much as patient response to chemotherapy varies, in this study both tissues which were previously identified as overexpressing HER2 receptors during initial patient diagnosis demonstrate considerably more receptors than the normal, nonneoplastic tissue. Additionally, H&E-stained sections of all tissue samples have been included (Fig. 4 (d.)) to illustrate the microscopic characteristics and differences associated with neoplastic vs. nonneoplastic conditions.

Summary

The macroscopic evaluation of resected tissue is currently the standard of practice for certain patients undergoing breast conservation therapy at tertiary centers, such as MDACC. As mentioned previously, this occurs primarily for non-palpable breast cancers (Cabioglu et al., 2007). Furthermore, this extra level of evaluation is not as common in community-based hospitals. Here, we demonstrate the ability to use targeted gold nanoshells to rapidly improve visualization of a specific biomarker associated with disease aggression and progression (HER2) in intact *ex vivo* human breast tissue. By utilizing silica-gold nanoshells designed as rapid

diagnostic imaging agents, surgeons and pathologists may be able to realize tumor margin status directly in the operating room after both macroscopic and microscopic assessment.

The ability to enhance contrast of malignancy using topically-applied agents has previously been demonstrated for oral tissue using fluorescently-labeled deoxy-glucose and epidermal growth factor (EGF) conjugates (Nitin et al., 2009a; Nitin et al., 2009b) as well as cervical tissue using fluorescently-labeled gold nanoparticles targeted to EGF receptors (Aaron et al., 2007). However, these studies employed incubation times ranging from 30-45 minutes, which exceeds the length of time currently needed to obtain tumor margin status using frozen section histology. Additionally, the aforementioned studies which evaluated malignancy based on EGF expression utilized optical clearing agents, which may be necessary for particles which target intracellular biomarkers (Ven et al., 2009a, b). Nevertheless, gold nanoshells targeted to extracellular biomarkers may offer more favorable opportunities for *ex vivo* intraoperative tumor margin detection without the need for lengthy incubation times or the use of optical clearing agents.

Recently, we verified that silica-based gold nanoshells could be used to enhance contrast of both HER2-overexpressing cells and tissue sections within 5 minutes of incubation time (Bickford et al., 2008a; Bickford et al., 2010). We take these findings one step further and confirm that these particles, when targeted to anti-HER2 receptors, can also be used to distinguish intact HER2-overexpressing *ex vivo* tissue from normal tissue within the same incubation time. Moreover, these results are supported by microscopic imaging with a reflectance confocal microscope as well as immunohistochemistry against HER2.

In order to translate these findings more readily to the clinic, we are presently developing a low cost widefield imaging system (Project 2) that can be used to detect the overexpression of HER2 (and other extracellular biomarkers) on account of contrast enhancement provided by gold nanoshells. In addition, we plan to collect data from diverse patient populations and assess results with fresh tissue samples. In this way, the use of gold nanoshells may demonstrate widespread efficacy or be limited only to specific patient subsets.

Our research indicates that *ex vivo* tissue specimens labeled topically with silica-based gold nanoshells can be visualized by both widefield (macroscopic) and high resolution (microscopic) imaging systems. By employing macroscopic imaging intraoperatively, clinicians may be better able to distinguish cancerous and non-cancerous breast tissue prior to further

microscopic analysis and subsequent histological processing. Ultimately, this system could also be used for other diagnostic applications, for other anatomical locations, and for other biomarkers associated with disease. By facilitating fast and accurate tumor margin results intraoperatively and supplementing current diagnostic methods, the incidence of cancer progression and amount of time spent in surgery due to inadequate tissue removal is, correspondingly, expected to be reduced.

(II) Technical Updates for Projects

Project 1 Technical Update

Over the past year, the needle compatible probe system has been modified with a new illumination source arrangement, which has proved very valuable in terms of layout and ease of adjustment (Figure 5). Please see the included *Journal of Biomedical Optics* paper for a review of the needle-based system and prior illumination design. Three degrees of translational adjustment and two degrees of angular adjustment are now possible in the new arrangement. The major benefit to imaging relative to our prior design is that because the entire optical pathway from illumination to detection is well aligned, system sensitivity has improved greatly. The only drawback is the heat generated by the LED, which cannot be dissipated by a heat sink and a fan as was the case in the prior design. The heat is transferred to the P100-P angular adjuster (to which the LED is heat taped) which becomes hot in a matter of minutes. This issue is currently being addressed. However, as long as the LED doesn't burn out, system performance isn't affected.

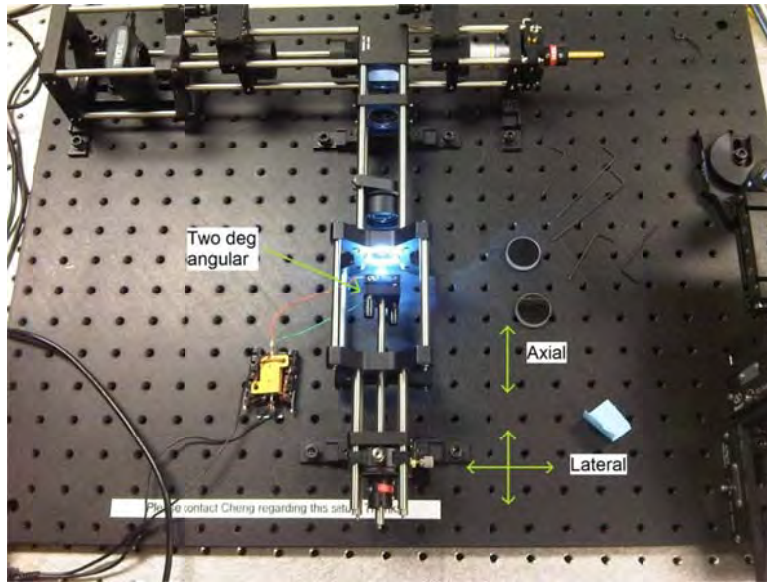
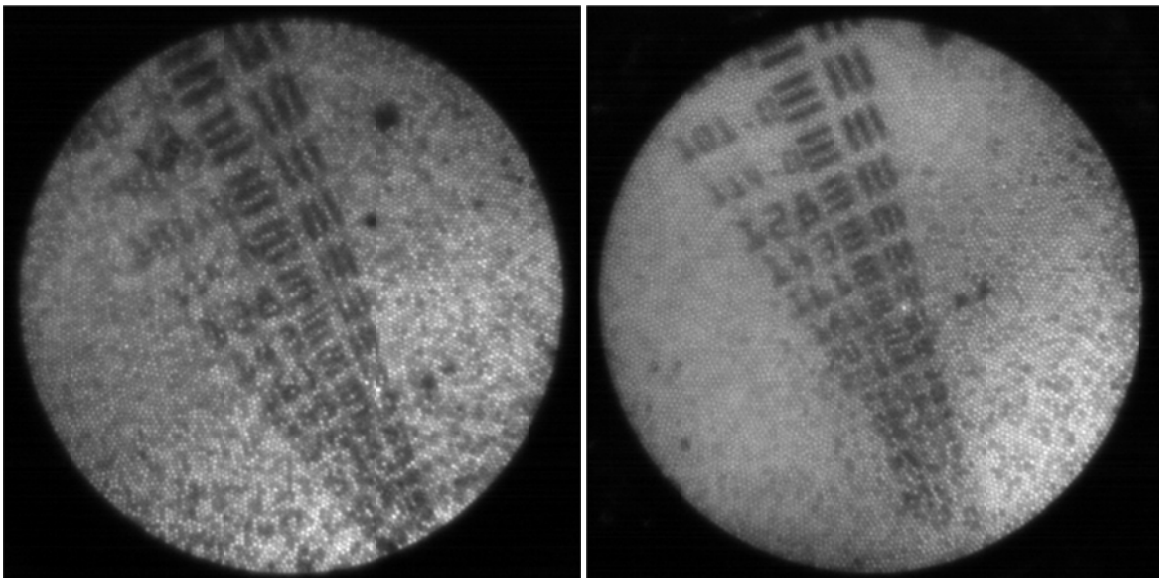


Figure 5: Photograph of the new illumination arrangement.

The improved performance of the system can be seen in the latest images of the USAF resolution target (Figure 6). With only 0.261 ms exposure time, very clear images can capture at resolutions in excess of 141 cycles/mm ($\sim 7 \mu\text{m}$). Polishing of the fiber has improved the image quality even more. However, it is still not at the point where the dark fiber cores are completely removed most likely due to an uneven image guide surface).



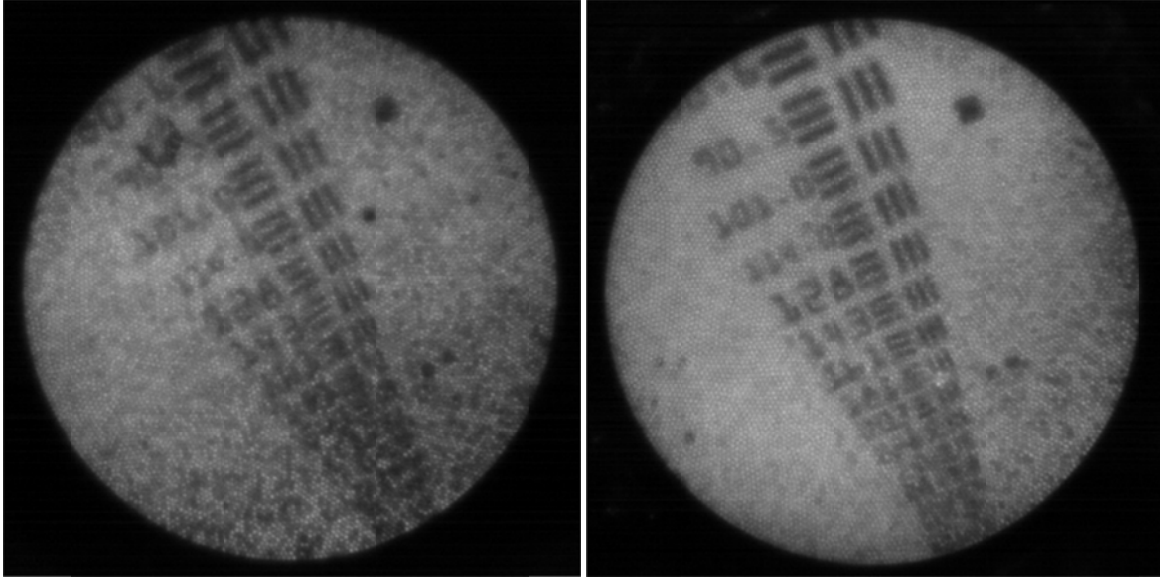


Figure 6: (Top left) Before polishing, with probe tip pressed against target; the dark dots corresponding to uneven image guide surface are clearly visible all over the image. (Bottom left) Before polishing, with the probe tip slightly above the target; the dark dots are not as prominent but still a major factor. (Top right) After polishing for 5 min, probe tip pressed against target; the dark dots are still present but not as intrusive. (Bottom right) After polishing and with probe tip slightly lifted, resolution as high as 181 cycles/mm (5.5 μ m) can be seen without interference from the black dots. Even though lifting the probe tip up slightly reduces the effect of the uneven image guide surface, the best resolution still occurs when the probe is pressed directly against the target. With a sufficiently smooth surface that removes all the black dots, even greater resolution may be attained. A droplet of water is used for index matching in all imaging cases; the exposure times are 0.261 ms in all cases.

Project 2 Technical Update

In our Year 3 report, we described the design of our first generation wide-field macroscopic system. One challenge with the first system was that it was not as portable as we would like for the application we ultimately envision: guiding breast tumor resection. Here, we briefly review already existing widefield imaging system and then describe design of the second generation system. In Year 5, we will finish constructing this system and assess performance using ex vivo breast cancer specimens.

There have been several different fluorescence imaging devices developed to improve cancer diagnostics. Most have focused on improving oral cancer detection because of the ease of tissue acquisition due to patients only having to open their mouth (Lane et al., 2006; Nitin et al., 2007; Roblyer et al., 2008; Roblyer et al., 2009). Tanaka et al. developed a system that combined

near infrared (NIR) fluorescence with white light to improve sentinel lymph node mapping (Tanaka et al., 2006). Additionally, the Maestro CRI imaging system has been used for *ex vivo* margin delineation (Nitin et al., 2009b) and *in vivo* cancer detection in mice (Ntziachristos et al., 2003; Sheth et al., 2009; Zhou et al., 2009). Fluorescence spectroscopy has also been used to evaluate the excitation and emission spectrums of *ex vivo* ovarian tissue (Brewer et al., 2001).

Currently, there are only two studies that combine the use of fluorescent contrast agents with wide-field imaging systems (Nitin et al., 2007; Nitin et al., 2009b). Other current wide-field imaging systems that have been published have only been designed to detect changes in autofluorescence that are seen in neoplastic tissue. Other studies that have involved contrast agents have been used for higher resolution systems such as confocal fluorescence and fiber-optic probes (Pierce et al., 2008; Bickford et al., 2009; Rosbach et al., 2010).

The project reported on at the beginning of our Year 4 report has demonstrated that the light scattering of large anti-HER2 targeted silica-gold nanoshells can be imaged using a wide-field stereoscope to differentiate HER2+ cancerous tissue from HER2- tissue. However, the stereoscope is expensive, large, and not portable. There is a need for the development of a portable, inexpensive, wide-field imaging system that has the capability of imaging these nanoshells. This system must also address the need for a wide-field imaging system that can image fluorescent contrast agents in conjunction with the nanoshells. This system will have the capacity to image multiple markers (such as Epidermal Growth Factor Receptor and HER2), the two markers we are targeting in Project 3. The system will also be able to used so that one imaging mode (such as fluorescence) validates the findings of the other mode (i.e. targeted silica-gold nanoshells). Below, we describe the system design we propose as well as the experiments we will complete in Year 5 to assess the system.

Design of Second Generation System

Camera

In order to capture the signal from nanoshells and fluorescent contrast agents, the camera must be able to acquire signal in both the visual spectrum of light (350-750 nm) and the NIR (750-1400 nm). To satisfy this parameter and maintain a low cost, a Canon 450D digital SLR camera was purchased and the IR filter inside the camera was removed for a total cost of \$1,095.00. Additionally, a camera lens with a focal length range of 18-55 mm (f/3.5-5.5) was purchased separately for a price of \$215.00.

Additionally, filters will be attached to the camera so that signal from the desired contrast agents will be collected and other signal, such as tissue scattering will be blocked. A Long Pass 780 nm (LP780) filter was purchased so that signal from the targeted silica-gold nanoshells could be collected, and a Bandpass Filter (500-560 nm) was purchased to detect signal from fluorophores that emit in the green spectrum. These two filters will attach to the end of the camera lens to block light emitted from the tissue samples before signal collection by the camera. The two filters were purchased for a total price of \$221.00. This leads to a total purchase price of the camera system to be \$1,531.00.

Excitation Source

A proper excitation wavelength and source is necessary to get maximum emission from the targeted contrast agents. In order to keep costs down and control the excitation wavelength, light emitting diodes (LEDs) were chosen to illuminate the sample and contrast agents. LEDs with different emission spectra can be purchased at a small price and arranged in a simple circuit so that the excitation sources can be controlled very simply. For the preliminary experiments, two sets of LEDs were chosen, Blue LEDs with an excitation peak of 465 nm (to excite green fluorophores such as FITC and 2-NBDG) and NIR LEDs with an emission peak of 851 nm to image the silica-gold nanoshells that have a Plasmon of 840 nm. These LEDs are available for a price of \$4.55 and \$3.75 each, helping to keep costs down.

Preliminary experiments have shown that unequal illumination of the samples leads to skewed results because the signal is highest where the light was hitting the sample. This has led to the concept of 360-degree illumination of the samples so that the sample is properly illuminated from all angles. Our design will follow the basic concept of the VisiLED MC1000 light source used in previous work; however, the illumination system will be modified for the camera lens. As well, our setup will have two different sets of LEDs, the Blue and the NIR, whose illumination will be controlled by a switch. The desired contrast agent and biomarker will determine which set of LED's will be illuminated.

Setup

A black, non-reflective stage for the tissues will be attached to a vertical metal pole. The tissue samples will be placed in the middle of the stage for sampling. The camera will be attached to the vertical pole so that it is perpendicular to the imaging stage with the lens facing downwards. This allows for camera stability and keeps the field of view constant from sample to sample. The

illumination device will be placed around the tissues and turned on, the respective filter for the desired contrast agent will be placed, and the image will then be acquired.

System Settings

The system's settings will need to be tested and optimized for both the fluorophore and nanoshells that will be targeting HER2+ breast tissue. The fluorophore that we will be testing the system with is FITC (fluorescein isocyanate), a common fluorophore. To test the FITC, 1 ml of 200 μ M FITC will be placed in a non-fluorescent glass embryo dish and illuminated with the Blue LEDs; excitation light will be filtered using the bandpass filter. Camera and illumination settings will be varied and the setting that gives the maximum signal will be used.

Additionally, settings for imaging non-targeted silica-gold nanoshells will also be determined by placing a 100 μ l of nanoshells onto a glass slide, illuminating the particles with NIR LEDs, and filtering the scattered light using the LP780 filter. Imaging conditions and settings will be varied as with the FITC, and images will be analyzed to determine which condition produces the highest signal.

Tissue Testing

Once the system's optimal settings have been determined, its imaging capability will be tested in frozen *ex vivo* breast cancer specimens. HER2-targeted silica-gold nanoshells will be used to discriminate HER2+ and HER2- tissue. These nanoshells will be synthesized following our previous work; however in place of the normal PEG-SH that has previously been added, FITC-PEG-SH will be added so that nanoshell presence can be secondary confirmation of nanoshell presence.

Tissue samples will be acquired from the Cooperative Human Tissue Network (CHTN). Both HER2+ and HER2- cancerous tissue will be acquired in addition to noncancerous tissue. The anti-HER2 nanoshells will incubate with the tissues for five minutes at 37°C then rinsed with cold PBS. Each type of tissue will also be incubated with PBS for a negative control. The tissues will be imaged using the system; each image will have one tissue incubated with nanoshells and one with PBS. The images will first be acquired using the NIR LEDs with the LP filter and then with the blue LEDs and the bandpass filter. The images will be processed using the image processing software ImageJ. The signal from the images will be converted to red (nanoshells) or green (FITC) and the images will be overlayed to compare the signal from the same tissue. The signal will also be quantitated using the values acquired from ImageJ. These

values will give us quantitative confirmation to the visual evidence that the targeted nanoshells selectively bound themselves to HER2+ cancerous tissue and not to HER2- tissue. Once imaged, the tissues will be frozen and sliced using a Leica tissue slicer (Leica CM 1850 UV). They will then be stained with an H&E stain and an immunohistochemical stain will be performed to test for the presence of the HER2 receptor.

This design will yield a portable inexpensive imaging system that has the potential to image multiple contrast agents. This system will be able to use multiple agents that can help optically differentiate cancerous tissue from non-cancerous tissue, via biomarkers, metabolic activity, or other hallmarks of malignant tissue. This system can be designed to work in concert with any contrast agent/marker combination. In addition, it is portable, inexpensive, and rapid. It will give clinicians a visual representation of tissue in the amount of time to take and process a normal digital photograph.

Project 3 Technical Update

Alternative Approach to Synthesis of NIR quantum dots

As noted in earlier reports, we have reduced our efforts using quantum dots as imaging agents relative to those using gold nanoparticles based on feedback from the last Era of Hope meeting suggesting that even cadmium-free quantum dots would find little patient acceptance for *in vivo* application. Because tumor margins can be checked directly after removal of the tissue, no *in vivo* use is required. This is the application of quantum dots we are still considering. We would like to compare results from both types of imaging agents being developed in this project: targeted gold nanoparticles and quantum dots. For optimal results, we require quantum dots with longer wavelength emission than those we described in the past which were originally intended for an *in vivo* imaging application. The synthesis protocol we are now using involves a reaction between lead acetate trihydrate and a sodium sulfide solution in the presence of thioglycerol and/or dithioglycerol to coat and stabilize the quantum dots. First, lead acetate was added to the

solution, and thioglycerol or dithioglycerol was added to prevent the formation of sodium hydroxide in a basic solution. The pH of the solution was then increased to 11.2 by adding triethylamine, any extra dithioglycerol was added, and then a .1 molar solution of sodium sulfide was then quickly injected into the system upon vigorous stirring. Altering the amount of thioglycerol and dithioglycerol introduced into the system greatly influenced the quality of the product, as well as the location of the emission peak. Furthermore, a smaller injection of sodium sulfide reduced clumping and aggregation in the product. We found that injecting 10 μL of sodium sulfide provided a clean and usable product.

We also found that adding more dithioglycerol into the solution blueshifted the emission peak and pushed it closer to around 950 nanometers, while adding thioglycerol redshifted the emission peak and pushed it towards 1250 nanometers. However, adding too much dithioglycerol produced clumping and aggregation, especially around the sides of the test tube. Furthermore, the inclusion of a thioglycerol coating stabilized the product and produced a significantly higher emission peak. Using a .6 mmol of dithioglycerol and 60 μL of thioglycerol coating produced an emission peak around 1050 nanometers, while reducing the thioglycerol to 5 μL produced a slightly weaker emission peak around almost exactly 1000 nanometers as shown below.

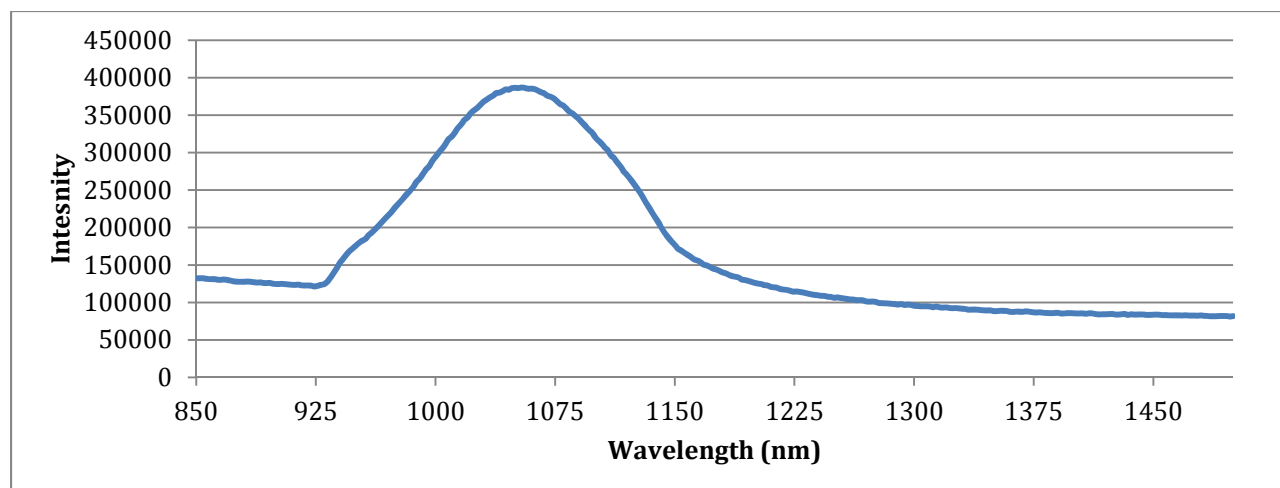


Figure 7: Emission spectra of NIR quantum dots (.6 mmol DTG, 60 μ L TGL, 10 μ L sodium sulfide, excited at 488 nm).

Continued Work on Development of Gold Nanoparticle Based Molecular Imaging Agents

An addition to our work in Project 3 over the past year was adding in an additional form of molecular contrast beyond the surface receptors originally proposed (HER2 and EGFR). This was based on a suggestion made to us at last year's LINKS meeting to broaden beyond targeting surface markers and to consider methods which could probe metabolism. Below, we provide some background on our approach to this problem, present initial data, and describe the steps we will take over the coming year to more fully assess the proposed new agents.

Targeted gold nanoparticles have been utilized to provide contrast for cell surface receptors such as Epidermal Growth Factor Receptor (EGFR) (Sokolov et al., 2003; El-Sayed et al., 2005) and for nuclear targeting (Tkachenko et al., 2003; Sun et al., 2008) for the past decade. The major means of imaging AuNPs have been demonstrated by Sokolov et al. whose work showed that gold nanoparticles could be imaged using confocal reflectance microscopy, and El-Sayed who illustrated the feasibility of darkfield imaging of gold nanoparticles (Sokolov et al., 2003; El-Sayed et al., 2005). A 2008 study by Kong et al. conjugated glucose to 10.8 nm (average) diameter AuNPs in order to improve cellular uptake of the nanoparticles to increase radiation cytotoxicity (Kong et al., 2008). Glucose-AuNP uptake was compared to bare NPs and NPs conjugated with cysteamine (AET-AuNPs) that attached to the cell surface. Results indicated that AET-AuNPs had the highest binding affinity to the cells. Transmission electron microscope (TEM) images showed that AET-NPs were localized to the cell surface whereas Glu-AuNPs had transversed the cell membrane and were found in the cytoplasm (Kong et al., 2008).

This led to an increased radiation cytotoxicity of Glu-AuNPs when compared to AET-NPs. Most importantly, Kong was able to increase the targeting rate of Glu-AuNPs versus the bare AuNPs, purportedly due to the increased metabolic activity of cancerous cells, which would mean the Glu-AuNPs would have to enter the cells via the glucose transporters (GLUTs). However, the researchers incubated the cells for a time period of 2 hours; this is more than enough time for the cells to ingest the NPs via clathrin mediated endocytosis (Connor et al., 2005; Mironava et al., 2010), phagocytosis (depending on the size of the NP) (El-Sayed et al., 2005; Mironava et al., 2010), or cell membrane mediated diffusion (Geiser et al., 2005). As well, the targeted nanoparticles had a very large size (10.8 nm) to be able to cross the cell membrane via GLUTs. Salas-Burgos et al. reports that the dimensions of the protein to be 36 X 26 Å on the extracellular side of the protein and 46 X 27 Å on the cytosolic side (Salas-Burgos et al., 2004), much smaller than the nanoparticles reported by Kong et al. This demonstrates that there is need to examine the mechanism of entry of glucose conjugated nanoparticles and determine the maximum size of a particle that can enter via the glucose transporter. The goal of this work is to determine the mechanism of entry and determine if glucose does enhance targeting of nanoparticles to breast cancer.

Glucose-Gold Nanoparticle Synthesis

AuNPs (~1.5 nm diameter) were synthesized using the following steps. 45 ml of deionized water was stirred with a stir bar at 700 rpm. 1 ml of 1M KOH was added to the water and stirred for 2 minutes. 12 µl of THPC was then added and stirred for 90 seconds. 2 ml of 1% HAuCl₄ was added and the solution was stirred for 5 minutes. Then, 60 µl cysteamine hydrochloride was added to the solution as a capping agent, and the solution was stirred in the dark for 2 hours. The solution was then stored at 20°C until further processing.

To remove excess cysteamine, 500 µl of the nanoparticles were pipetted into a 3,500 Dalton molecular weight cutoff dialysis membrane. The solution was then dialyzed for 48 hrs with the dialysis buffer (deionized H₂O) being replaced at 2, 4, 24, and 48 hours to remove excess cysteamine for the conjugation process. Once the solution was dialyzed, the absorbance of the solution was read from 240-700 nm (data presented in Figure 5). To link the glucose to the AuNP, an EDC-NHS zero length linker was used to link the D-glucose to the cysteamine capping the particle. EDC-NHS is a common linker used to link nanostructures (Wu et al., 2007) via the amine group of the cysteamine that is covering the nanoparticle.

D-glucose was added to a solution containing EDC and sulfo-NHS. The EDC replaced the hydrogen of the –OH group bound to C1 of glucose. Sulfo-NHS was used to stabilize the product so that it did not revert to normal glucose, creating a quasi-stable active ester that reacted with the –NH group of the cysteamine on the AuNPs (Staros et al., 1986). The Glucose-EDC-NHS was then added to the AuNPs and reacted for 2 hours at room temperature in the dark. Once the reaction was completed, absorbance readings of the nanoparticles were taken (data presented in Figure 8). Preliminary data confirmed conjugation of glucose to the AuNPs because of the red shift seen in the spectrum of the particles after conjugation. However, further post conjugation steps, such as removal of excess glucose-EDC-NHS from solution need to be optimized so that the particles are ready to be added to the cells.

Experiments to be Conducted in Year 5

Cellular Experiments

After the conjugation procedure has been optimized, conjugated and non-conjugated particles will be added to the SkBr3 breast cancer cell line to test the targeting ability of glucose conjugated nanoparticles (Glu-AuNPs). Approximately 500,000 cells will be plated on a tissue culture treated microscope slide for 48 hours. After 48 hours, cell culture media will be removed and 1% bovine serum albumin in PBS will be added to the cells for 20 minutes to starve the cells. Glu-AuNPs will be added for 20 minutes at 37°C and then rinsed with PBS to remove any excess nanoparticles. A 20 minute incubation time is chosen due to previous cellular experiments with fluorescent deoxy-glucose (2-NBDG) that displayed uptake of the fluorophore within that time frame (O'Neil et al., 2005). Individual cells will be examined under a darkfield

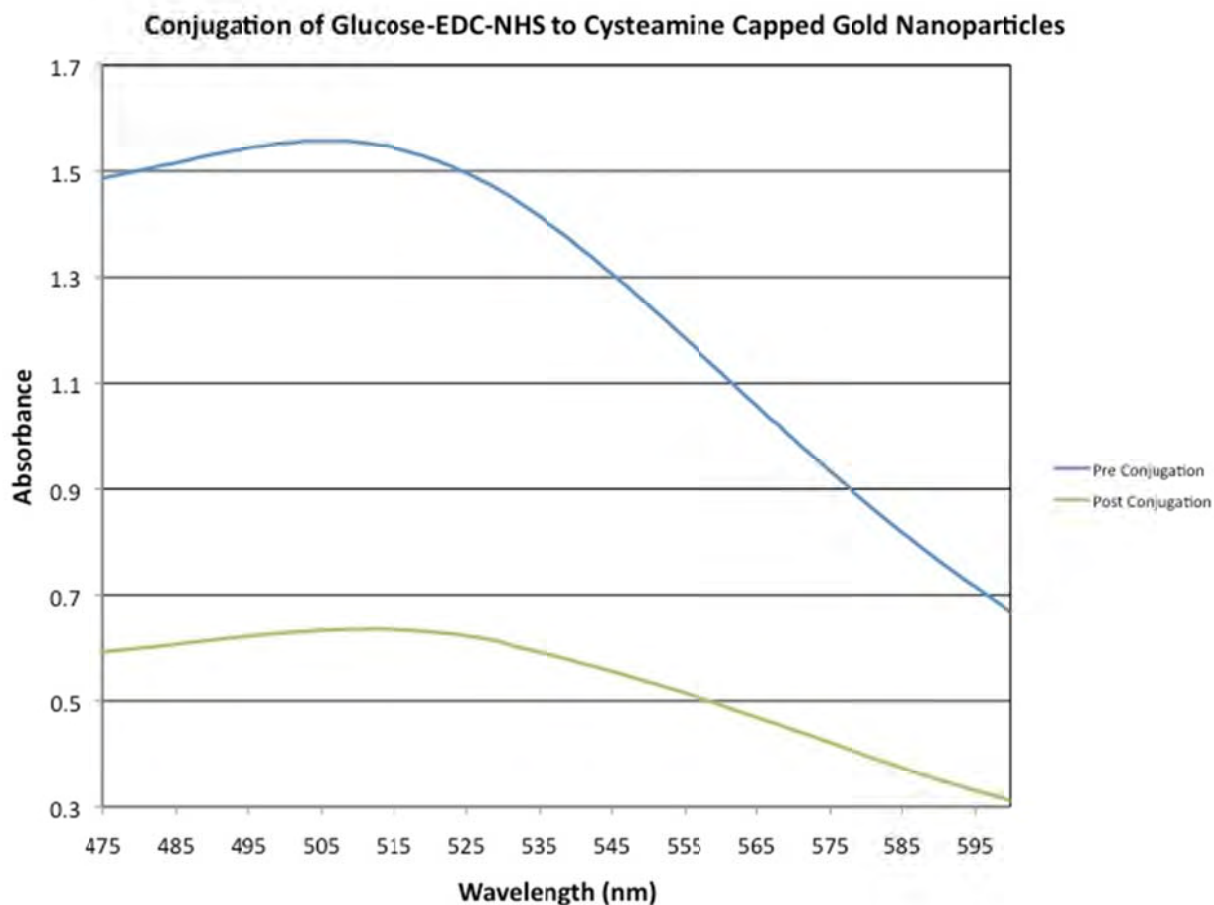


Figure 8. Absorption spectra of cysteamine capped gold nanoparticles before and after conjugation with Glucose-EDC-NHS. The absorbance peak of the particles before conjugation was 505 nm and for post conjugation it was 512 nm, confirming conjugation. The absorbance of the conjugated nanoparticles is much lower because the sample was diluted by 50% when added to the glucose-EDC-NHS solution.

microscope using a 100X objective to locate the particles' location with respect to the cell. In addition to acquiring qualitative image data, hyperspectral data of each image will also be acquired. The hyperspectral data will allow us to analyze the scattering profile of the nanoparticles and determine if the particles have entered the cell, or if they have only accumulated along the cell membrane. Hyperspectral data will also allow us to determine if particles have aggregated inside the cell. Final confirmation of cellular uptake will be completed by taking high-resolution TEM images of the cells as was presented by Kong (Kong et al., 2008). High-resolution and hyperspectral imaging will allow us to determine a difference between targeted and non-targeted particles and allow for future experiments to determine mechanism of entry.

Once cellular uptake of the targeted nanoparticles has been confirmed, multiple assays will be run to determine how the particles entered the cell. The first assay will optically determine if the Glu-AuNPs have entered the cells via endocytosis. Endosomal DNA of the SkBr3 cells will be transfected with red fluorescent protein (RFP) and cells will be prepared as previously described. Conjugated nanoparticles will be added in the same procedure as the previous step and imaged using the same darkfield setup. In addition to the normal darkfield image captured, the microscope can be switched to darkfield fluorescence mode so that the RFP labeled endosomes can be imaged. As well, hyperspectral images of both the darkfield and fluorescent images will be acquired under the same setup. The information from these images will allow us to localize nanoparticles and endosomes which will allow us to determine if nanoparticles are being endocytosed.

A second experiment to independently confirm that the Glu-AuNPs do not enter the cell via endocytosis will be to block endosomal formation using sodium azide, as presented by Chithrani et al. (Chithrani et al., 2007). In this experiment, cells will once again be cultured and plated as in previous studies, however they also will be treated with sodium azide as an endosomal blocking compound. Once the cells are treated, conjugated and non-conjugated nanoparticles will once again be added to the cells for 20 minutes and then rinsed with PBS. The cells will once again be imaged using a darkfield microscope and hyperspectral information will also be recorded. If data shows that there are nanoparticles inside the cells, this will be a second validation that they did not enter the cells via endocytosis, and further investigation into how the particles entered the cell will be necessary.

The previous experiments will not be enough to confirm how the nanoparticles enter the cell. We hypothesize that Glu-AuNPs will enter via the GLUT1 transporter; however, to prove this hypothesis, a competition assay with D-glucose is necessary. Studies by O'Neil and Nitin have demonstrated decreased uptake of fluorescent deoxy-glucose (2-NBDG) when both 2-NBDG and D-glucose were added to the same batch of MCF-7 cancerous cells (O'Neil et al., 2005; Nitin et al., 2009a). These studies concluded that 2-NBDG entered the cells via the GLUT1 glucose transporter because the uptake of the fluorophore was competitively inhibited with the presence of D-glucose. Using this concept, glucose conjugated AuNPs and D-glucose will be added to the same batch of cells in a competition assay similar to the assay performed by O'Neil and Nitin. Cells will be plated for 48 hours and treated as in previous studies. However,

this time a combination of D-glucose and Glu-AuNPs will be added to the cells; as well, there will be a control of only AuNPs and a control of D-glucose only added to cells so that a qualitative and quantitative comparison can be made. Cells will once again be imaged under darkfield microscopy; additionally hyperspectral data of the cells will be acquired for further comparison. If it is determined that D-glucose inhibited the entry of nanoparticles into the cancerous cells, then that will further elucidate the mechanism of entry for glucose conjugated gold nanoparticles.

The final experiment will be to determine how the different sizes of the gold nanoparticles affects the entry of the bioconjugate into the cell. Due to the small size of GLUT1, it is hard to envision large nanoparticles being able to cross the membrane through the small pore of the GLUT1. To determine the size limit, AuNPs of varying diameter (1.5, 3, 5, 10 nm) will be synthesized and capped with cysteamine as in previous experiments. SkBr3 breast carcinoma cells will be cultured and plated as outlined in previous steps; the cells will also be treated with sodium azide to inhibit the formation of endosomes so that we can ensure the larger particles do not enter via endocytosis. D-glucose will be added to the AuNPs as outlined in previous steps, and then they will be added to the cells in the same manner as previous experiments. Cells will then be imaged and hyperspectral information will be acquired as in previous steps. Information will be compared between images to determine if larger particles were able to enter the cell.

In summary, we aim to target small (~1.5 nm) gold nanoparticles using D-glucose to target the increased GLUT1 expression seen in breast cancer. We aim to elucidate the mechanism of entry of these particles into SkBr3 breast cancer cells to determine if glucose conjugated AuNPs have a future as an additional type of molecular imaging agents. We will then be able to directly visualize this agent using the wide-field instrument being developed in Project 2.

Overall Future Directions

Our previous work has demonstrated that we have the ability to differentiate cancerous breast tissue from noncancerous tissue using specific biomarker targeted nanoshells. Preliminary data also shows that large slices of *ex vivo* cancerous tissue can be incubated with contrast agents and imaged macroscopically imaged in a span of 10 minutes. One problem with the macroscopic imaging is the scattering signal from tissues is very high in the NIR range. The scattering is due

to the presence of water in the tissue that leads to mismatched indices of refraction between water, protein structures, and collagen (Liu et al., 1996). Future work will involve combining a method of “tissue clearing” to lower scattering and enhance signal seen from the targeted nanoshells. Clearing methods such as mechanical and chemical clearing developed by Rylander and Vargas (Vargas et al., 1999; Vargas et al., 2001; Rylander et al., 2008) will be explored as possible answers to removing endogenous tissue scattering, needed for both Projects 1 and 2.

The portable inexpensive imaging systems being developed in Projects 1 and 2, together with the targeted imaging agents in Project 3, have great potential for use to optically identify more than just breast cancer. They are generally relevant for imaging a wide spectrum of biomarkers associated with any type of cancer. The devices provide clinicians the ability to evaluate the heterogeneity of cancerous tissue optically, noninvasively, and rapidly. They provide the potential to give clinicians a fast, macroscopic image of cancerous and noncancerous tissue intraoperatively so that an informed decision may be made about whether negative margins have been achieved during surgery.

Personnel Note

One of our collaborators, Dr. Tse-Kuan Yu, has left M.D. Anderson Cancer Center for private practice. He is a radiation oncologist who had originally been involved in the award because of the nanoparticle radiation project proposed. This was the project (Project 4) we did not continue after 24 months because the results suggested we could not achieve measurements of clinically relevant radiation dosages, leading to the revised statement of work with this project only included for Years 1-2 rather than all 5 years. After ending the radiation sub-project, Dr. Yu remained involved in our HER2 nanoparticle targeting efforts. Since leaving M.D Anderson, he has continued to collaborate with us on publishing the projects we have worked on together.

KEY RESEARCH ACCOMPLISHMENTS

- As noted in our Year 3 report, we received approval from Rice University and DoD for an exemption protocol for acquisition of breast tissue from the NCI Cooperative Human Tissue Network so that we could test our imaging systems and agents using more biologically relevant samples. This allowed us to conduct a series of tissue studies in Year 4 providing preliminary results demonstrating the potential clinical utility of the methods and imaging agents being developed. As we expected, critical issues to ultimate clinical implementation, such as the impact of neoadjuvant chemotherapy on our proposed methods were able to be identified from working with human breast tissue samples rather than simpler mimics.
- We have continued to improve performance of the needle compatible system for microscopic, high resolution imaging (United States provisional patent submitted) incorporating an improved illumination set up over the past reporting period (**Project 1**)
- We have continued development of the macroscopic imaging system suitable for visualization of large regions of the breast at once. In Year 3, we demonstrated the first generation device. In Year 4, we have designed and began assembly of the second generation device. This is designed to be a handheld device surgeons could ultimately use to guide tumor resection. (**Project 2**)
- We have synthesized cadmium-free NIR quantum dots for molecular targeted fluorescence imaging at wavelengths high enough that there will not be interference from autofluorescence (**Project 3**)
- We have designed a new type of layered nanoparticle which we envision to be of particular use for multiplexed molecular imaging. The particles consist of a gold core, silica middle layer, and outer gold shell with the core offset with respect to the center of the particle, providing ability to sculpt optical properties to meet specific design criteria (**Project 3** – described in ACS Nano paper)
- We have begun assessment of glucose conjugated gold nanoparticles as a means to assess metabolic activity in order to broaden the range of molecular features of cancer we are able to probe. This work was initiated in response to a suggestion received at the DoD LINKS meeting. (**Project 3**)

REPORTABLE OUTCOMES

Peer Reviewed Journal Papers

Sun, J., C. Shu, et al. (2010). "Needle-compatible single fiber bundle image guide reflectance endoscope." J Biomed Opt **15**(4): 040502. (A Word document of the version of this manuscript in place prior to publication was submitted in last year's report. This year we include the published paper.)

Hu, Y., Noelck, S., and Drezek, R. "Symmetry breaking in gold-silica-gold multilayer nanoshells." ACS Nano. 4(3): 1521-1528 (2010).

Carpin, L. B., L. R. Bickford, et al. (2011). "Immunoconjugated gold nanoshell-mediated photothermal ablation of trastuzumab-resistant breast cancer cells." Breast Cancer Res Treat **125**(1): 27-34.

Abstracts

Bickford, L., and Drezek, R. Gold-silica nanoshells for targeted imaging of tumor margins. Biomedical Engineering Society Annual National Meeting. Austin, TX. October 2010.

Langsner, R., Yu, K., and Drezek, R. The Use of 2-NBDG for Optical Assessment of Breast Tumor Margins. Biomedical Engineering Society Annual National Meeting. Austin, TX. October 2010.

Noelck, S. and Drezek, R. Optical Properties of Gold-Silica-Gold Nanoshells. Biomedical Engineering Society Annual National Meeting. Austin, TX. October 2010.

Noelck, S., Hu, Y., and Drezek, R. Probing Optical Properties of Gold-Silica-Gold Multilayer Nanoshells with Broken Symmetry, 2010 Inter IGERT Nanoscience and Professional Development Workshop. Austin, TX. 2010.

Langsner, R., Drezek, R. and Yu, K. Towards 2-NBDG for Intraoperative Assessment of Tumor Margins. Gordon Conference on Lasers in Surgery and Medicine. 2010.

Other Presentations

Drezek, R. Nanotechnology Enabled Optical Molecular Imaging of Cancer. DoD Links Meeting. 2011. Small group presentations.

Jobs

Dr. Jiantang Sun, a postdoctoral fellow funded by this project, became an Associate Professor at the Chinese Academy of Sciences Suzhou Institute of Biomedical Engineering

Dr. Lissett Bickford, a graduate student who worked on this project, completed her PhD degree

in Biomedical Engineering and joined the cancer nanotechnology lab of Dr. Joe DeSimone, a NIH Pioneer Award winner

Awards

Robert Langsner, a graduate student funded by this project, received the 2010 Edgar O'Rear Travel Award for conference travel support

CONCLUSIONS

Our research team, comprised of my group at Rice and MDACC collaborators, is focusing the majority of its Era of Hope research efforts specifically in areas of breast cancer care where the combination of *miniaturized optical devices* and *molecular-specific imaging agents* offer the potential to address current gaps in care. There are two primary areas where I believe our technologies can make the biggest difference: *early detection* and *monitoring therapy*. Optical spectroscopy, implemented through small fiber optics, can provide clinically valuable information ranging from cellular metabolic status (via endogenous fluorescence) to nuclear size (correlated to optical scatter) to quantitative measurements of molecular markers (through targeted imaging agents under development in our lab). Most of our effort has focused on development of needle-compatible spectroscopic and direct imaging probes for breast cancer applications. The technology is being designed for clinical applications for which it is valuable to have a local high resolution imaging method to complement a more macroscopic imaging modality (for example, during ultrasound guided breast biopsy). Progressive design and evaluation of these needle-based technologies is **Project 1** of our DOD project. Important milestones over the past year include the publishing in the top biomedical optics journal, *Journal of Biomedical Optics*, of our first paper in this area (accepted at the time of our last report) and additional design improvements to our device which may yield additional intellectual property in addition to the provisional patent reported last year. In Year 3, we added in a new project, **Project 2**, to allow us to further develop a multi-modal, widefield optical imaging device; in Year 4, we have focused on design of a hand held version of this device specifically optimized for breast tumor margins assessment. To complement our imaging technology development projects, the second primary effort underway is development of molecular-specific optical imaging probes (**Projects 3**). Many similar probes developed to date have been suitable for lab-based but not clinical work. A challenge of most NP-based molecular contrast methods has been that conventional imaging protocols require incubation periods of over one hour. This is not clinically viable for either for our diagnostic or monitoring applications. During Year 1, we developed protocols for imaging of HER2 which preserves ~90% of optical contrast at 10 minutes. The fast imaging times we have been able to achieve open up the possibility of another type of breast cancer monitoring application: tumor margins assessment. Especially in community hospital settings, there is a critical need for new technologies for rapid intraoperative margins assessment. To be viable, a complete procedure must be accomplished in under 15-20 minutes. Much of the work already underway in **Project 3** has been directly applicable to tumor margins assessment, and we presented our initial tissue results in this Year 4 report with final results expected in Year 5.

REFERENCES

- Aaron, J., N. Nitin, et al. (2007). "Plasmon resonance coupling of metal nanoparticles for molecular imaging of carcinogenesis in vivo." J Biomed Opt **12**(3): 034007.
- Bickford, L., G. Agollah, et al. (2009). "Silica-gold nanoshells as potential intraoperative molecular probes for HER2-overexpression in ex vivo breast tissue using near-infrared reflectance confocal microscopy." Breast Cancer Research and Treatment: 1-9.
- Bickford, L., G. Agollah, et al. (2010). "Silica-gold nanoshells as potential intraoperative molecular probes for HER2-overexpression in ex vivo breast tissue using near-infrared reflectance confocal microscopy." Breast Cancer Research and Treatment **120**(3): 547-555.
- Bickford, L., J. Chang, et al. (2008a). "Evaluation of Immunotargeted Gold Nanoshells as Rapid Diagnostic Imaging Agents for HER2-Overexpressing Breast Cancer Cells: A Time-based Analysis." NanoBioTechnology **4**(1): 1-8.
- Bickford, L. and et al. (2008b). "Enhanced multi-spectral imaging of live breast cancer cells using immunotargeted gold nanoshells and two-photon excitation microscopy." Nanotechnology **19**(31): 315102.
- Brewer, M., U. Utzinger, et al. (2001). "Fluorescence spectroscopy for in vivo characterization of ovarian tissue." Lasers Surg Med **29**(2): 128-135.
- Buckman, R. (1997). What You Really Need to Know About Cancer. Baltimore, The Johns Hopkins University Press.
- Cabioglu, N., K. Hunt, et al. (2007). "Role for Intraoperative Margin Assessment in Patients Undergoing Breast-Conserving Surgery." Annals of Surgical Oncology **14**(4): 1458-1471.
- Cancer, S. A. (2005). "Breast Cancer Facts and Figures 2005-2006." Atlanta ACS, Inc.
- Chithrani, B. D. and W. C. W. Chan (2007). "Elucidating the Mechanism of Cellular Uptake and Removal of Protein-Coated Gold Nanoparticles of Different Sizes and Shapes." Nano Letters **7**(6): 1542-1550.
- Connor, E. E., J. Mwamuka, et al. (2005). "Gold Nanoparticles Are Taken Up by Human Cells but Do Not Cause Acute Cytotoxicity." Small **1**(3): 325-327.
- Duff, D. G., A. Baiker, et al. (1993). "A new hydrosol of gold clusters. 1. Formation and particle size variation." Langmuir **9**(9): 2301-2309.
- El-Sayed, I. H., X. Huang, et al. (2005). "Surface plasmon resonance scattering and absorption of anti-EGFR antibody conjugated gold nanoparticles in cancer diagnostics: applications in oral cancer." Nano Lett **5**(5): 829-834.
- Fisher, B., S. Anderson, et al. (2002). "Twenty-Year Follow-up of a Randomized Trial Comparing Total Mastectomy, Lumpectomy, and Lumpectomy plus Irradiation for the Treatment of Invasive Breast Cancer." New England Journal of Medicine **347**(16): 1233-1241.
- Geiser, M., B. Rothen-Rutishauser, et al. (2005). "Ultrafine particles cross cellular membranes by nonphagocytic mechanisms in lungs and in cultured cells." Environ Health Perspect **113**(11): 1555-1560.
- Graham, R. A., M. J. Homer, et al. (1994). "The efficacy of specimen radiography in evaluating the surgical margins of impalpable breast carcinoma." AJR Am J Roentgenol **162**(1): 33-36.
- Kong, T., J. Zeng, et al. (2008). "Enhancement of radiation cytotoxicity in breast-cancer cells by localized attachment of gold nanoparticles." Small **4**(9): 1537-1543.

- Lane, P. M., T. Gilhuly, et al. (2006). "Simple device for the direct visualization of oral-cavity tissue fluorescence." Journal of Biomedical Optics **11**(2): 024006-024007.
- Liu, H., B. Beauvoit, et al. (1996). "Dependence of tissue optical properties on solute-induced changes in refractive index and osmolarity." Journal of Biomedical Optics **1**(2): 200-211.
- Loo, C., L. Hirsch, et al. (2005a). "Gold nanoshell bioconjugates for molecular imaging in living cells." Opt Lett **30**(9): 1012-1014.
- Loo, C., A. Lin, et al. (2004). "Nanoshell-enabled photonics-based imaging and therapy of cancer." Technol Cancer Res Treat **3**(1): 33-40.
- Loo, C., A. Lowery, et al. (2005b). "Immunotargeted nanoshells for integrated cancer imaging and therapy." Nano Lett **5**(4): 709-711.
- Mironava, T., M. Hadjiargyrou, et al. (2010). "Gold nanoparticles cellular toxicity and recovery: Effect of size, concentration and exposure time." Nanotoxicology **4**(1): 120-137.
- Mojica CM, B. R., Boscardin WJ, Ponce NA (2007). "Low-Income Women with Breast Abnormalities: System Predictors of Timely Diagnostic Resolution." Cancer Control **14**(2): 176-182.
- Nahta, R., D. Yu, et al. (2006). "Mechanisms of disease: understanding resistance to HER2-targeted therapy in human breast cancer." Nat Clin Pract Oncol **3**(5): 269-280.
- Nitin, N., A. L. Carlson, et al. (2009a). "Molecular imaging of glucose uptake in oral neoplasia following topical application of fluorescently labeled deoxy-glucose." Int J Cancer **124**(11): 2634-2642.
- Nitin, N., D. J. Javier, et al. (2007). "Widefield and high-resolution reflectance imaging of gold and silver nanospheres." J Biomed Opt **12**(5): 051505.
- Nitin, N., K. J. Rosbach, et al. (2009b). "Optical molecular imaging of epidermal growth factor receptor expression to improve detection of oral neoplasia." Neoplasia **11**(6): 542-551.
- Ntziachristos, V., C. Bremer, et al. (2003). "Fluorescence imaging with near-infrared light: new technological advances that enable in vivo molecular imaging." Eur Radiol **13**(1): 195-208.
- O'Neil, R., L. Wu, et al. (2005). "Uptake of a Fluorescent Deoxyglucose Analog (2-NBDG) in Tumor Cells." Molecular Imaging and Biology **7**(6): 388-392.
- Oouchi, A., K.-i. Sakata, et al. (2009). "The treatment outcome of patients undergoing breast-conserving therapy: the clinical role of postoperative radiotherapy." Breast Cancer **16**(1): 49-57.
- Pierce, M. C., D. J. Javier, et al. (2008). "Optical contrast agents and imaging systems for detection and diagnosis of cancer." Int J Cancer **123**(9): 1979-1990.
- Rasbridge, S. A., C. E. Gillett, et al. (1994). "The effects of chemotherapy on morphology, cellular proliferation, apoptosis and oncoprotein expression in primary breast carcinoma." Br J Cancer **70**(2): 335-341.
- Roblyer, D., C. Kurachi, et al. (2009). "Objective detection and delineation of oral neoplasia using autofluorescence imaging." Cancer Prev Res (Phila Pa) **2**(5): 423-431.
- Roblyer, D., R. Richards-Kortum, et al. (2008). "Multispectral optical imaging device for in vivo detection of oral neoplasia." J Biomed Opt **13**(2): 024019.
- Rosbach, K. J., D. Shin, et al. (2010). "High-resolution fiber optic microscopy with fluorescent contrast enhancement for the identification of axillary lymph node metastases in breast cancer: a pilot study." Biomed. Opt. Express **1**(3): 911-922.

- Rylander, C. G., T. E. Milner, et al. (2008). "Mechanical tissue optical clearing devices: enhancement of light penetration in ex vivo porcine skin and adipose tissue." Lasers Surg Med **40**(10): 688-694.
- Salas-Burgos, A., P. Iserovich, et al. (2004). "Predicting the three-dimensional structure of the human facilitative glucose transporter glut1 by a novel evolutionary homology strategy: insights on the molecular mechanism of substrate migration, and binding sites for glucose and inhibitory molecules." Biophys J **87**(5): 2990-2999.
- Sheth, R. A., L. Josephson, et al. (2009). "Evaluation and clinically relevant applications of a fluorescent imaging analog to fluorodeoxyglucose positron emission tomography." J Biomed Opt **14**(6): 064014.
- Slamon, D. J., G. M. Clark, et al. (1987). "Human breast cancer: correlation of relapse and survival with amplification of the HER-2/neu oncogene." Science **235**(4785): 177-182.
- Smitt, M. C., K. W. Nowels, et al. (1995). "The importance of the lumpectomy surgical margin status in long term results of breast conservation." Cancer **76**(2): 259-267.
- Sokolov, K., M. Follen, et al. (2003). "Real-Time Vital Optical Imaging of Precancer Using Anti-Epidermal Growth Factor Receptor Antibodies Conjugated to Gold Nanoparticles." Cancer Res **63**(9): 1999-2004.
- Staros, J. V., R. W. Wright, et al. (1986). "Enhancement by N-hydroxysulfosuccinimide of water-soluble carbodiimide-mediated coupling reactions." Analytical Biochemistry **156**(1): 220-222.
- Steen, R. (1993). A Conspiracy of Cells. New York, Plenum Press.
- Stober, W., A. Fink, et al. (1968). "Controlled growth of monodisperse silica spheres in the micron size range." Journal of Colloid and Interface Science **26**(1): 62-69.
- Sun, L., D. Liu, et al. (2008). "Functional Gold Nanoparticle,àPeptide Complexes as Cell-Targeting Agents." Langmuir **24**(18): 10293-10297.
- Tanaka, E., H. S. Choi, et al. (2006). "Image-guided oncologic surgery using invisible light: completed pre-clinical development for sentinel lymph node mapping." Ann Surg Oncol **13**(12): 1671-1681.
- Tkachenko, A. G., H. Xie, et al. (2003). "Multifunctional Gold Nanoparticle,àPeptide Complexes for Nuclear Targeting." Journal of the American Chemical Society **125**(16): 4700-4701.
- Vargas, G., K. F. Chan, et al. (2001). "Use of osmotically active agents to alter optical properties of tissue: Effects on the detected fluorescence signal measured through skin." Lasers in Surgery and Medicine **29**(3): 213-220.
- Vargas, O., E. K. Chan, et al. (1999). "Use of an agent to reduce scattering in skin." Lasers in Surgery and Medicine **24**(2): 133-141.
- Ven, A. L. v. d., K. Adler-Storthz, et al. (2009a). "Delivery of optical contrast agents using Triton-X100, part 1: reversible permeabilization of live cells for intracellular labeling." Journal of Biomedical Optics **14**(2): 021012.
- Ven, A. L. v. d., K. Adler-Storthz, et al. (2009b). "Delivery of optical contrast agents using Triton-X100, part 2: enhanced mucosal permeation for the detection of cancer biomarkers." Journal of Biomedical Optics **14**(2): 021013.
- Wu, B.-Y., S.-H. Hou, et al. (2007). "Amperometric glucose biosensor based on multilayer films via layer-by-layer self-assembly of multi-wall carbon nanotubes, gold nanoparticles and glucose oxidase on the Pt electrode." Biosensors and Bioelectronics **22**(12): 2854-2860.

Zhou, L. and W. S. El-Deiry (2009). "Multispectral fluorescence imaging." J Nucl Med **50**(10): 1563-1566.

Needle-compatible single fiber bundle image guide reflectance endoscope

Jiantang Sun,^a Chenghao Shu,^a Benjamin Appiah,^b and Rebekah Drezek^{a,b,*}

^aRice University, Department of Bioengineering, 6100 Main Street, Houston, Texas 77005

^bRice University, Department of Electrical and Computer Engineering, 6100 Main Street, Houston, Texas 77005

Abstract. We developed a miniaturized high-resolution low-cost reflectance-mode fiber microscope (RFM) aimed at optical tissue biopsy applications using a polarized imaging configuration to suppress background noise from specular reflectance. The RFM is equipped with an air-cooled light-emitting-diode illumination module and a single 450- μm outer-diameter fiber bundle image guide compatible with a 20-gauge needle. The dual illumination and image acquisition nature of the fiber bundle simplifies the system and reduces the total cost. Imaging tests with a United States Air Force resolution target demonstrate a lateral resolution of $\sim 3.5\ \mu\text{m}$. The performance of the imaging system is evaluated by examining samples of cells and excised human tissue. Still and video rate images are obtainable in reflectance mode using intrinsic contrast. © 2010 Society of Photo-Optical Instrumentation Engineers. [DOI: 10.1117/1.3465558]

Keywords: reflectance fiber endoscope; optical biopsy.

Paper 10220LR received Apr. 26, 2010; revised manuscript received Jun. 11, 2010; accepted for publication Jun. 23, 2010; published on-line Jul. 29, 2010.

Standard pathology requires removal of cells or tissue through techniques ranging from fine needle aspiration or core needle biopsy to surgical resection. To allow examination of suspect lesions, a variety of endoscopic imaging techniques may be employed, including fiber-scanning confocal microscopy in reflectance^{1,2} and fluorescence³ modes. These techniques use an optical fiber or fiber bundle to view the surface of interior body cavities. Images are created by scanning mechanisms positioned at either the distal or proximal ends of the fiber. These types of systems can capture point-by-point high-resolution images from a large field of view, and the sensitivity of the systems can be very high.^{4,5} Recent advances provide similar high-resolution images using simple, low-cost systems based on coherent fiber bundles with images captured using inexpensive digital cameras.^{6–8} Image resolution is limited by the individual fibers of the fiber bundle. A fluorescence-mode fiber endoscope developed by Muldoon et al. achieves a resolution of $\sim 4.4\ \mu\text{m}$.^{6,7} We are developing a high-resolution ($\sim 3.5\ \mu\text{m}$) reflectance-mode endoscope that is flexible, compatible with a 20-gauge needle, and can generate

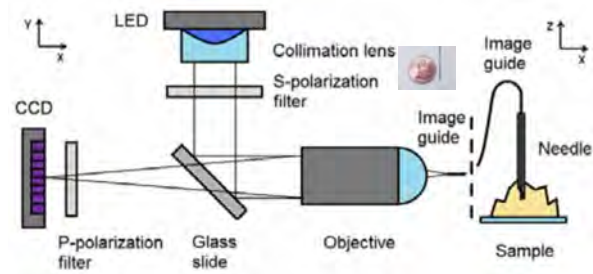


Fig. 1 Schematic of the reflectance fiber imaging system.

still and video rate images using intrinsic contrast. Reflectance-mode endoscopic imaging can potentially complement fluorescence imaging by capturing information not available in fluorescence mode, and by functioning in situations when fluorescent imaging is not practical.

In this work, we present a needle-based, high-resolution reflectance-mode fiber microscope (RFM) developed for optical tissue biopsy applications. The RFM was assembled on a portable $18 \times 24 \times 1/2$ in.³ aluminum breadboard to facilitate eventual clinical trials. As shown in Fig. 1, an air-cooled light-emitting diode (LED) (Luxeon, Brantford, Ontario, Canada; white LED, model LXHL-NWE8; blue LED, model LXHL-NRR8) served as the illumination source to keep the RFM as compact as possible and reduce the system cost. The light from the LED is collimated by an integrated collimating lens and passes through a linear polarizer (Fig. 1), after which the polarized light is reflected by a glass slide positioned at $\sim 45^\circ$ (with respect to the beam trajectory) and projected onto an infinity-corrected $10\times$ objective lens (Newport, Irvine, California, model L-10 \times , 0.25 NA). The objective lens and a fiber chuck (Newport, model FPH-DJ) are positioned with a multimode fiber-coupler positioner (Newport, model F-915T). By careful alignment, the illumination light is focused into the incident end of a 450- μm outer-diameter fiber bundle image guide positioned by the fiber chuck (Sumitomo Electric U.S.A., Los Angeles, California, model IGN-037/10, 10^4 fiber elements in a picture area of $333\ \mu\text{m}$ diameter, 0.35 NA).⁹ Finally, the imaging end of the fiber image guide is inserted into the core of a 20-gauge needle and positioned in contact with the samples. Light scattered from the samples is collected by the same illumination fiber and passes back through the same $10\times$ objective lens and glass slide described previously (see Fig. 1).

A charge-couple device (CCD) color camera (Edmund Optics, Barrington, New Jersey, model EO-0813C) coupled with a circular polarizer filter (Nikon, 62 mm) is used to sample the fiber bundle elements for image acquisition. Because the polarization orientation of the S-polarized illumination light is perpendicular to the plane of incidence with respect to the glass slide (i.e., the XY plane of Fig. 1), a significant portion is reflected toward the incident end of the fiber bundle to be delivered to the imaging end of the fiber bundle. Specular reflectance from the incident end of fiber bundle is also partly reflected away by the glass slide, and the remaining specular reflectance is further suppressed by the circular polarizer in front of the CCD camera that passes P-polarized light with

*Address all correspondence to: Rebekah Drezek, Tel: 713-348-3011; Fax: 713-348-5877; E-mail: drezek@rice.edu

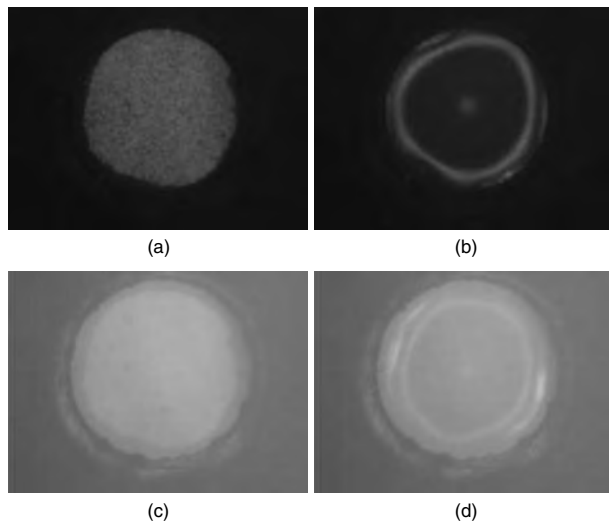


Fig. 2 Reflectance images of the fiber-bundle tip glass/air interface showing greatly reduced specular background using this RFM system in comparison with the nonpolarized imaging system. Images (a) and (b) were obtained using cross-polarized illumination and imaging filters. For image (a), the fiber tip was in air. For image (b), the fiber tip was covered with a drop of water. Images (c) and (d) were obtained without polarized illumination and imaging filters. Image (c) is with the fiber tip in air, whereas image (d) is with the fiber tip covered with a drop of water.

respect to the plane of incidence. Rays that result from multiple scattering events changing their polarization to the parallel direction can be detected by the CCD camera (e.g., light scattered from the sample). Thus, noise due to specular reflectance from the incident end of the fiber bundle is greatly suppressed, and clearer images are collected.

Figure 2(a) shows a reflectance image of the fiber bundle imaging end when the needle microscope is positioned in air. Light from the white LED that is reflected from the glass-air interface at the imaging end of the fiber bundle is successfully detected by the CCD camera, and individual fibers of the fiber bundle are resolved [Fig. 2(a)]. With the imaging needle of the RFM immersed into a vial of water or phosphate-buffered saline (PBS) solution, the RFM field of view is almost completely dark, because the close match between the refractive indices of water and the glass fiber result in dramatically reduced internal reflection from the imaging end of the fiber bundle.

Figure 2(b) is obtained with a drop of water covering the tip of the imaging fiber bundle, which mimics the immersion of the fiber tip in water, to provide clear image features. Much less internal reflection occurs from the imaging area covered by water [Fig. 2(b)] compared with the same area when it is exposed to air. Figures 2(a) and 2(b) were captured with the same imaging configurations and the index-matching effect is clear. When used in biological or clinical environments, the fiber bundle tip is always in contact with body fluids or tissue. Thus, dipping the fiber bundle tip into water roughly approximates the conditions of realistic imaging applications. In liquid, the reduced internal reflectance leads to a dark field of view and a decrease in background enabling biological imaging. Light scattered by biological structures can be clearly distinguished and cellular images can be obtained. In contrast to the polarized reflectance-mode images in Figs. 2(a) and

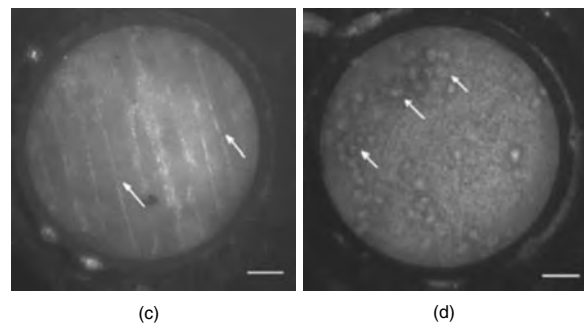
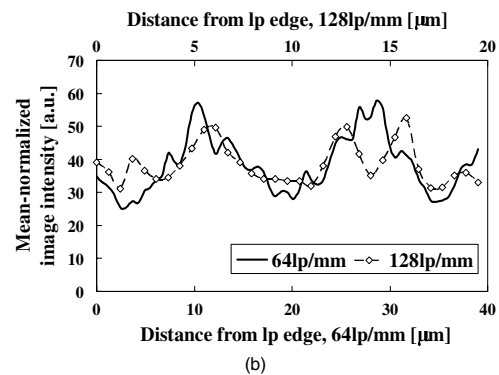
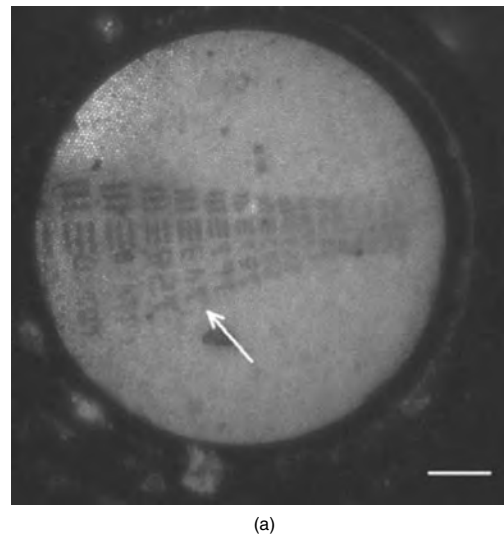


Fig. 3 Processed endoscopic imaging results of (a) USAF resolution target showing the resolution of ~ 143 lp/mm, acquired with white LED illumination, (b) cross sections of two resolution line-pair sets showing both the line-pair intensity variation and variation due to probe fibers ($3.3 \mu\text{m}$ diam), (c) onion skin cells (see also Video 1), where arrows show the resolved cell walls acquired with white LED illumination, and (d) cultured SKBR3 cancer cells (see also Video 2), where the arrows indicate resolved single cells acquired with blue LED illumination. Scale bar is $50 \mu\text{m}$. (Video 1, QuickTime, 754 KB [URL: <http://dx.doi.org/10.1117/1.3465558.1>]; Video 2, QuickTime, 977 KB [URL: <http://dx.doi.org/10.1117/1.3465558.2>].)

2(b), images shown in Figs. 2(c) and 2(d) were captured with a reduced exposure time under the same imaging conditions, but without the illumination and collection polarizers. The specular reflectance from the optical components makes it impossible to obtain useful information from Figs. 2(c) and 2(d).

A white LED was used to acquire the images and plots

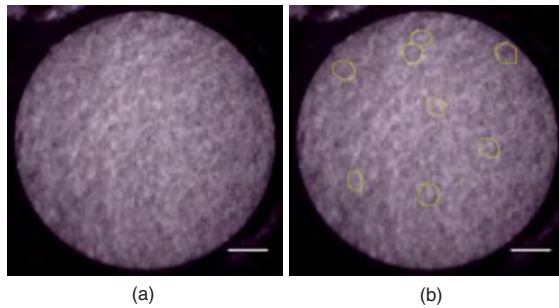
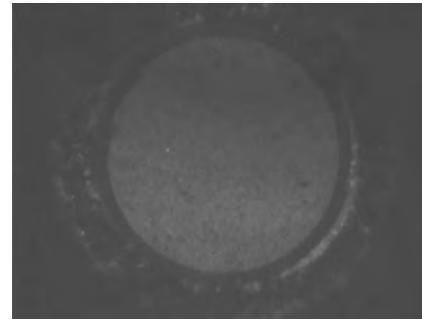


Fig. 4 Endoscopic images of excised oral cancer tissue including (a) processed image showing cellular structures (see also [Video 3](#), where images move in and out of focus as the imaging tip moves), and (b) processed images with drawn lines superimposed to indicate the estimated cell boundaries. Scale bar is 50 μm . ([Video 3](#), QuickTime, 2.12 MB [[URL: http://dx.doi.org/10.1117/1.3465558.3](http://dx.doi.org/10.1117/1.3465558.3)].)

shown in Figs. 3(a)–3(c) and [Video 1](#). Figure 3(a) shows an imaging resolution of $\sim 3.5 \mu\text{m}$ (~ 143 line pairs/mm) obtained upon imaging the United States Air Force resolution target. Figure 3(b) shows that contrast decreases slightly from low (64 lp/mm) to high (128 lp/mm) resolution, but it also reveals high-frequency components due to the probe fibers (3.3 μm diam). Figure 3(c) and [Video 1](#) were obtained by using the same white LED-illuminated RFM to image skin tissue from a green onion. The cell walls of the rectangular green onion skin cells¹⁰ are clearly resolved in both the still image and the video. Note that water was used in all the tests to provide refractive index matching.

The LED light source is cost effective and easy to change. An air-cooled blue LED was used to image cultured SKBR3 human carcinoma cells. Before imaging, SKBR3 carcinoma cells were cultured in a 6-mm plate at 37 °C for 2 days. The fiber bundle tip was immersed into the culture medium through a needle and focused onto a group of cells attached to the culture plate. As shown in Fig. 3(d), the cells can be visualized with the RFM using blue-LED illumination. An endoscopic video clip of the SKBR3 cancer cells is provided in [Video 2](#). The same RFM was also used to image excised human oral cancer tissue obtained from the Cooperative Human Tissue Network (CHTN, Rockville, Maryland). The tissue was placed in a culture plate with PBS, which was then placed on a 2-D translation stage. The needle and fiber bundle tip were inserted into the tissue sample, and cellular structures were visualized as shown in Fig. 4 and [Video 3](#). In [Video 3](#), cellular images move in and out of focus as the imaging tip moves closer to or further away from the sample. The same RFM was used to image the reflectance from a dust particle in liquid solution to demonstrate single pixel fiber resolution, as shown in [Video 4](#).

In this work, we describe a high-resolution RFM developed for optical tissue biopsy applications. The resolution of this fiber microscope is limited by the element fiber size of the imaging fiber bundle. For the specific fiber bundle image guide presented, the resolution is $\sim 3.5 \mu\text{m}$. The reported RFM system uses the same fiber bundle guide for both illumination and imaging. A pair of cross-polarized filters is used in addition to the fiber bundle guide to achieve high-resolution reflectance-mode microscopic imaging. The fiber bundle guide is 450 μm in diameter, making it compatible



Video 4 Reflectance endoscopic video of a dust particle in liquid solution showing single pixel fiber resolution. (QuickTime, 950 KB). [[URL: http://dx.doi.org/10.1117/1.3465558.4](http://dx.doi.org/10.1117/1.3465558.4)].

with current clinical needle tissue biopsy systems. The RFM system can be used without external agents when there is sufficient endogenous imaging contrast. Moreover, with simple filter changes, the RFM system can readily be converted to a fluorescence-mode needle biopsy imaging system similar to that developed by Muldoon et al.⁶ Future work will assess whether performance can be improved through the use of simple chemical agents already in routine clinical use.

Acknowledgments

The authors gratefully acknowledge support from the Department of Defense Congressionally Directed Breast Cancer Research Program Era of Hope Scholar Award (W81XWH-07-1-0428). The NCI Cooperative Human Tissue Network (CHTN) provided specimens used in this project.

References

1. C. Liang, M. Descour, K. B. Sun, and R. Richards-Kortum, "Fiber confocal reflectance microscope (FCRM) for in-vivo imaging," *Opt. Express* **9**, 821–830 (2001).
2. K. C. Maitland, A. M. Gillenwater, M. D. Williams, A. K. El-Naggar, M. R. Descour, and R. R. Richards-Kortum, "In vivo imaging of oral neoplasia using a miniaturized fiber optic confocal reflectance microscope," *Oral Oncol.* **44**, 1059–1066 (2008).
3. F. Jean, G. Bourg-Heckly, and B. Viellerobe, "Fibered confocal spectroscopy and multicolor imaging system for in vivo fluorescence analysis," *Opt. Express* **15**, 4008–4017 (2007).
4. V. Dubaj, A. Mazzolini, A. Wood, and M. Harris, "Optic fiber bundle contact imaging probe employing a laser scanning confocal microscope," *J. Microsc.* **207**, 108–117 (2002).
5. R. Kiesslich, M. Goetz, M. Vieth, P. R. Galle, and M. F. Neurath, "Technology Insight: confocal laser endoscopy for in vivo diagnosis of colorectal cancer," *Nat. Clin. Pract. Oncol.* **4**, 480–490 (2007).
6. T. J. Muldoon, M. C. Pierce, D. L. Nida, M. D. Williams, A. Gillenwater, and R. Richards-Kortum, "Subcellular-resolution molecular imaging within living tissue by fiber microendoscopy," *Opt. Express* **15**, 16413–16423 (2007).
7. T. J. Muldoon, S. Anandasabapathy, D. Maru, and R. Richards-Kortum, "High-resolution imaging in Barrett's esophagus: a novel, low-cost endoscopic microscope," *Gastrointest. Endosc.* **68**, 737–744 (2008).
8. T. J. Muldoon, N. Thekkekk, D. Roblyer, D. Maru, N. Harpaz, J. Potack, S. Anandasabapathy, and R. Richards-Kortum, "Evaluation of quantitative image analysis criteria for the high-resolution microendoscopic detection of neoplasia in Barrett's esophagus," *J. Biomed. Opt.* **15**, 026027 (2010).
9. Sumitomo Electric U.S.A., Image Guide Technical Document (<http://www.sumitomoelectricusa.com/scripts/products/ofig/image.cfm>) (2010).
10. A. G. von Arnim, X. W. Deng, and M. G. Stacey, "Cloning vectors for the expression of green fluorescent protein fusion proteins in transgenic plants," *Gene* **221**, 35–43 (1998).

Immunoconjugated gold nanoshell-mediated photothermal ablation of trastuzumab-resistant breast cancer cells

Laura B. Carpin · Lissett R. Bickford ·
Germaine Agollah · Tse-Kuan Yu · Rachel Schiff ·
Yi Li · Rebekah A. Drezek

Received: 4 February 2010 / Accepted: 13 February 2010
© Springer Science+Business Media, LLC. 2010

Abstract Trastuzumab is a FDA-approved drug that has shown clinical efficacy against HER2+ breast cancers and is commonly used in combination with other chemotherapeutics. However, many patients are innately resistant to trastuzumab, or will develop resistance during treatment. Alternative treatments are needed for trastuzumab-resistant patients. Here, we investigate gold nanoparticle-mediated photothermal therapies as a potential alternative treatment for chemotherapy-resistant cancers. Gold nanoshell photothermal therapy destroys the tumor cells using heat, a physical mechanism, which is able to overcome the cellular adaptations that bestow trastuzumab resistance. By adding anti-HER2 to the gold surface of the nanoshells as a targeting modality, we increase the specificity of the nanoshells for HER2+ breast cancer. Silica-gold nanoshells conjugated with anti-HER2 were incubated with both

trastuzumab-sensitive and trastuzumab-resistant breast cancer cells. Nanoshell binding was confirmed using two-photon laser scanning microscopy, and the cells were then ablated using a near-infrared laser. We demonstrate the successful targeting and ablation of trastuzumab-resistant cells using anti-HER2-conjugated silica-gold nanoshells and a near-infrared laser. This study suggests potential for applying gold nanoshell-mediated therapy to trastuzumab-resistant breast cancers in vivo.

Keywords Nanoshells · Photothermal therapy · Chemotherapy resistance · Breast cancer · Trastuzumab

Introduction

Despite the advances in the treatment of early-stage breast cancer, patients with advanced Stage III and IV disease have 5-year survival rates of only 57% and 20%, respectively [1]. Although many new chemotherapy drugs and regimens have been developed, little improvement has been seen in the ultimate outcome of these cancer patients. Epidermal growth factor 2 receptor (Erb2 or HER2) is amplified in 20–25% of human breast cancer, and is known to be a marker of poorer prognosis due to HER2+ breast cancers aggressive nature and tendency to recur [2, 3]. In 2006, a therapeutic antibody against HER2 (Trastuzumab) was developed as part of a new class of drugs. Trastuzumab binds to the HER2 receptor and halts tumor cell growth through suppression of HER2 signaling and subsequent elevation of the levels of p27^{KIP1} protein [2]. Trastuzumab showed positive clinical results as a treatment for HER2+ metastatic breast cancer in clinical trials [4, 5], and after subsequent studies was approved as a treatment for patients with HER2+ metastatic breast

L. B. Carpin · L. R. Bickford · T.-K. Yu · R. A. Drezek (✉)
Department of Bioengineering, Rice University, 6100 Main St.,
MS-142, Houston, TX 77005, USA
e-mail: drezek@rice.edu

G. Agollah
Nanospectra Biosciences Inc., Houston, TX 77054, USA

T.-K. Yu
Department of Radiation Oncology, The University of Texas
M.D. Anderson Cancer Center, Houston, TX 77030, USA

R. Schiff · Y. Li
Breast Center, Baylor College of Medicine, Houston, TX 77030,
USA

R. A. Drezek
Department of Electrical and Computer Engineering, Rice
University, Houston, TX 77005, USA

cancer. Despite the initial success of trastuzumab, the development of drug resistance has presented a major barrier. The majority of patients are intrinsically resistant to trastuzumab prior to starting therapy [6], and most initially responsive patients develop resistance to treatment within a year [2]. Second generation agents like lapatinib, which is small molecule-based tyrosine kinase inhibitor, have been developed for trastuzumab-resistant patients, but chemotherapy resistance continues to be problematic [7]. The development of gold nanoparticle-mediated photothermal cancer therapy presents a new and minimally invasive treatment possibility for chemotherapy-resistant cancers [8]. To date, gold nanoparticle-mediated treatment has only been applied to chemotherapy-sensitive cell lines. Here, we demonstrate the targeting and photothermal ablation of trastuzumab-resistant breast cancer cells in vitro using anti-HER2-conjugated silica–gold nanoshells.

The development of trastuzumab resistance has been attributed to a variety of mechanisms, including overexpression of glycoprotein MUC4 [9], overexpression of insulin-like growth factor 1 (IGF-1) [10], and constitutive PI3K/Akt activity [11]. However, even in cases where there is obstructed binding of the extracellular component of the HER2 receptor, the receptor itself remains unchanged. In addition, although a mutation of the extracellular component of the HER2 receptor that results in trastuzumab resistance is theoretically possible, in most cases of resistance this does not occur [2]. This presents the possibility of using an antibody generated against the HER2 receptor as a targeting modality for an alternative form of therapy, such as gold nanoparticle-mediated photothermal therapy.

Gold nanoparticles have great potential in the diagnosis, management, and treatment of cancer due to their versatile scattering and absorbing properties, as well as the ease with which their surfaces can be modified. For therapy applications, a variety of gold nanoparticles can be used, including gold colloid [12], silica–gold nanoshells [8], gold nanorods [13], and gold nanocages [14]. For this study, silica–gold nanoshells are used due to their low cytotoxicity profile and demonstrated efficacy as a therapeutic against HER2+ breast cancer cells [8, 15, 16]. Gold nanoshells usually consist of a dielectric core, such as silica, which is coated with a thin layer of gold. The unique optical properties of nanoshells are due to the localized surface plasmon resonance of the gold metal electrons, and these properties can be modulated by controlling the thickness of the gold coating during synthesis. When designed to primarily absorb light, nanoshells can efficiently convert light energy to heat energy, destroying adjacent cells via thermal ablation [15, 17–19]. Unlike conventional hyperthermia treatments, the use of nanoshells as an absorptive agent has the

added benefit of decreasing the laser intensity requirements for therapy, which prevents inadvertent ablation of normal cells.

To further enhance therapy, ligands such as antibodies, polymers, or DNA, can be conjugated to the gold nanoparticle surface. This modification has demonstrated increased target specificity in vitro [8, 17, 20]. In the case of HER2+ breast cancer, Loo et al. demonstrated that gold–silica nanoshells conjugated to anti-HER2 can be successfully used to target and ablate chemotherapy-sensitive breast cancer cells in culture [16]. Here, we demonstrate that anti-HER2-conjugated silica–gold nanoshells can mediate effective targeting and photothermal ablation of two cultured anti-HER2-resistant breast cancer cell lines—JIMT-1 has a lower level of anti-HER2 binding due to overexpression of MUC4 [9], and BT474 AZ LR is resistant to both trastuzumab and lapatinib. Using photothermal therapy, the cancer cells can be destroyed by the conversion of nanoshell-absorbed energy to heat. This physical mechanism of cell ablation effectively evades any developed intracellular resistance mechanism, presenting a new possibility for the treatment of trastuzumab-resistant breast cancers.

Methods

Breast cancer cell lines

Three HER2-overexpressing breast cancer cell lines were chosen for this study: SK-BR-3, JIMT-1, and BT474 AZ LR. The MCF10A cell line, which is an immortalized, HER2 negative breast epithelial cell line, was used as a control. The SK-BR-3 and MCF10A cell lines were purchased from American Type Culture Collection. The SK-BR-3 cell line is trastuzumab sensitive. The JIMT-1 cell line was purchased from DSMZ (Germany), and is trastuzumab resistant. The BT474 AZ LR cell line, a subculture of BT474, is resistant to both trastuzumab and lapatinib. The SK-BR-3 and JIMT-1 cell lines were both cultured in McCoy's 5A and Dulbecco's Modified Essential Medium, respectively, supplemented with 10% fetal bovine serum (FBS) and 1% penicillin–streptomycin. The BT474 AZ LR cell line was cultured in Dulbecco's Modified Essential Medium High Glucose supplemented with 10% FBS and 1% penicillin–streptomycin–glutamine and with 1 μ M of lapatinib to maintain HER2 therapy resistance. The MCF10A cells were cultured in Mammary Epithelial Basal Medium (MEBM) supplemented with a BulletKit (Clonetics). All cells were maintained at 37°C in a 5% CO₂ atmosphere.

Quantification of HER2 receptor antigens on cell surface

Quantification of HER2 surface receptors was performed as described by Bickford et al. [21]. Cells were grown to confluence, trypsinized, counted, and incubated with either media alone, PE antihuman CD340 (erbB2/HER-2) antibody (BioLegend, San Diego, CA), or PE mouse IgG1 isotype control antibody (BioLegend, San Diego, CA) for 30 min on ice in the dark. The IgG1 isotype serves as background signal correction. The cells were then washed in $1 \times$ PBS, resuspended in 500 μ l of cell staining buffer (BioLegend, San Diego, CA, USA), and stored on ice until analysis. Immunofluorescence intensity was determined by flow cytometry at The University of Texas M.D. Anderson Cancer Center (MDACC) flow cytometry core. To correlate the immunofluorescence intensity with the quantity of HER2 antigens available for binding on each cell, a Quantum Simply Cellular anti-Mouse IgG kit (Bangs Laboratories, Inc., Technology Drive Fishers, IN, USA) was used. This kit has four different sets of microbeads possessing a known number of antigen binding sites, which permits the development of a calibration curve correlating immunofluorescence intensity with the quantity of antigen binding sites. The curve is then used to calculate the number of antigen binding sites per cell.

Silica-gold nanoshells and antibody conjugation

The silica-gold nanoshells were synthesized using previously described methods [15–17, 22]. In brief, silica cores were created using the Stöber method [23], and the silica core surface was functionalized with amine groups. These amine groups were then used to seed 4–7-nm gold colloid onto the silica surface. The size of the silica cores was determined to be 120 nm by scanning electron microscopy (SEM) prior to gold seeding. The gold shell was then completed by adding additional gold solution, potassium carbonate, and formaldehyde. After synthesis, the UV–Vis spectrum of the nanoshells was correlated with Mie Theory to determine the absorption, extinction, and scattering coefficients of the nanoshells, and subsequently the approximate concentration. The average nanoshell diameter was confirmed to be 150 ± 10 nm by SEM. The nanoshell peak absorbance was determined to be 780 nm with a concentration of 3.85×10^9 nanoparticles/ml (Fig. 1).

To modify the surfaces of the nanoshells with anti-HER2 antibody, the methods of Loo et al. were employed [16]. The anti-HER2 antibody (C-erbB-2/HER-2/neu Ab-4, Lab Vision Corporation) was incubated with a custom orthopyridyl-disulfide-polyethylene glycol-*N*-hydroxysuccinimide ester (OPSS-PEG-NHS, MW = 2kD, CreativeBiochem Laboratories, Winston Salem, NC, USA) linker at a molar ratio of

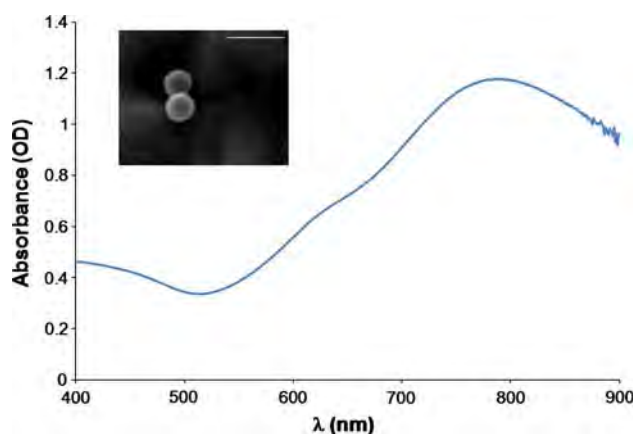


Fig. 1 Absorbance spectrum of the silica-gold nanoshells (silica core radius = 60 nm, total radius = 75 nm). Inset shows SEM image of the nanoshells; scale bar is 300 nm

3:1 in sodium bicarbonate (100 mM, pH 8.5) overnight on ice at 4°C. Aliquots were then stored at –80°C until use, when they were thawed on ice. The antibody binds to the OPSS-PEG-NHS linker via the amide group, and adsorbs to the gold surface of the nanoshell via the thiols of the OPSS group. To attach the antibody-linker to the gold nanoshells, nanoshells were incubated with the antibody-linker at 4°C for 2 h, then 1 mM polyethylene glycol-thiol (PEG-SH, MW = 5kD, Nektar) was added and the nanoshells were incubated overnight at 4°C for further stabilization. After nanoshell conjugation, the unreacted PEG-linker and PEG-SH were removed by centrifugation of the nanoshell solution and removal of the supernatant. The anti-HER2 nanoshells were then resuspended in cell-line appropriate media prior to use in cell studies.

Two-photon laser scanning microscopy to confirm binding efficiency

For in vitro two-photon nanoshell binding studies, 5×10^5 cells in suspension from each cell line (MCF10A, SK-BR-3, JIMT-1, and BT474 AZ LR), were incubated with 1.73×10^9 nanoshells in 1 ml of media for 1 h at 37°C with rotation in a hybridization oven. Cells incubated with media alone were used as a control. After the incubation, the cell lines were washed three times with 1 ml of $1 \times$ phosphate-buffered saline (PBS) to remove unbound nanoshells, and resuspended in 0.5 ml of cell line appropriate media. Each treatment and control group was then seeded onto an inverted coverslip and allowed to attach overnight. A Zeiss Laser Scanning Microscope 510 META multiphoton system (Zeiss, Thornwood, NY, USA) was used in combination with a Coherent Chameleon femto-second mode locked Ti:sapphire laser (Coherent, Santa Clara, CA, USA) for imaging.

Nanoshell-mediated photothermal therapy

For in vitro photothermal ablation studies, 5×10^5 cells in suspension from each cell line (MCF10A, SK-BR-3, JIMT-1, and BT474 AZ LR) were incubated with 1.71×10^{10} nanoshells as described above. Media alone was again used as a control. Cells were washed with PBS and seeded in coverslips as described above.

Laser irradiation of the cells was performed in a similar manner to previous photothermal therapy studies [16–18]. After the cells were attached, each well was uncovered, placed on top of a glass microscope slide, and exposed to an 808-nm NIR diode laser (Coherent Inc., Santa Clara, CA, USA) at 80 W/cm^2 with a 1.5-mm spot size for 5 min.

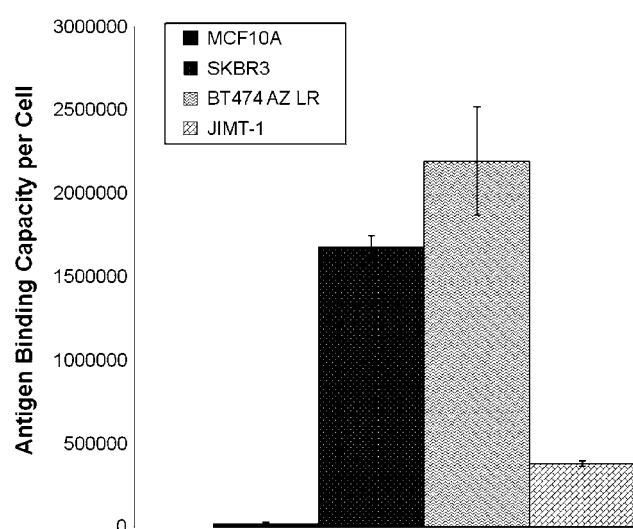
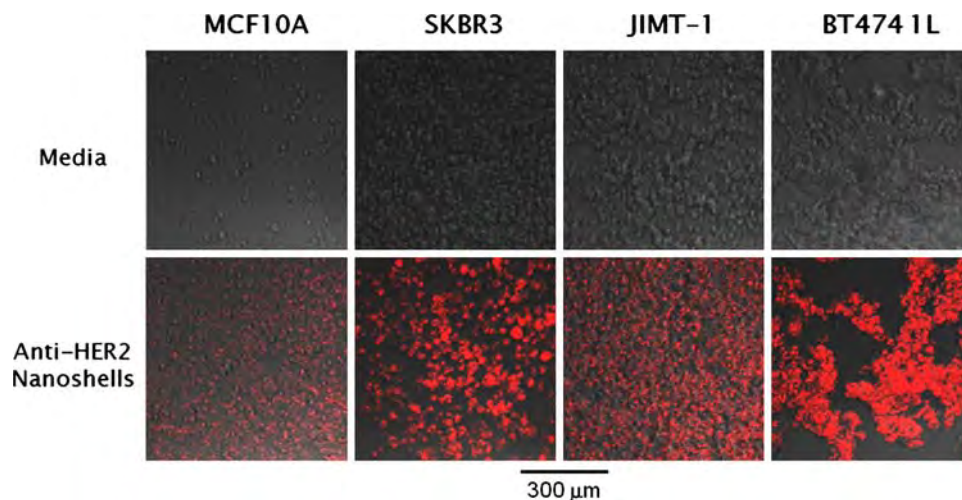


Fig. 2 Anti-HER2 binding capacity of each breast cancer cell line, determined by flow cytometry. The HER2+ cell lines (SK-BR-3, JIMT-1, BT474 AZ LR) show a significantly higher binding capacity than the HER2-cell line (MCF10A). Data for MCF10A, SK-BR-3, and JIMT-1 reused with permission from [21]. Copyright 2009 from Springer

Fig. 3 Verification of nanoshell binding using two-photon laser scanning microscopy. Images depicted are phase contrast images overlaid with two-photon images. SK-BR-3, JIMT-1, and BT474 AZ LR cell lines, all HER2+, show greater binding of the anti-HER2 nanoshells than the MCF10A normal epithelial cell line



Following laser irradiation, the cells were returned to the 37°C incubator with 5% CO_2 for several hours. Live/dead viability staining was then performed using an Invitrogen Live/Dead viability/cytotoxicity kit (Carlsbad, CA, USA), and cells were imaged using a Zeiss Axiovert 135 Fluorescence microscope (Zeiss, Thornwood, NY, USA). To confirm nanoshell binding, silver staining was performed using Sigma–Aldrich Silver Enhancement solutions (St. Louis, MO, USA), followed by brightfield imaging.

Results

Quantification of antigen binding for each cell line

Using flow cytometry, the number of antigen binding sites for each cell line was determined, as displayed in Fig. 2. Data for the MCF10A, SK-BR3, and JIMT-1 cell lines are being reused with permission from [21]. A one-factor ANOVA test indicated significant differences between cell lines in the number of binding sites ($P < 0.01$). Each of the HER2+ breast cancer lines used in this study had a larger number of anti-HER2 binding sites than the normal epithelial cell line, MCF10A ($2.43 \times 10^4 \pm 3.77 \times 10^3$ receptors), by the Tukey comparison test ($P < 0.01$). The BT474 AZ LR cell line had the greatest anti-HER2 binding capacity ($2.19 \times 10^6 \pm 3.25 \times 10^5$ receptors), followed by the SK-BR-3 ($1.68 \times 10^6 \pm 6.78 \times 10^4$ receptors) and then the JIMT-1 ($3.82 \times 10^5 \pm 1.47 \times 10^4$ receptors) cell lines. Notably, the JIMT-1 cell line has a significantly lower HER2 binding site expression when compared to the SK-BR-3 and BT474 AZ LR cell lines ($P < 0.01$).

Two-photon microscopy of nanoshell–cell binding

Nanoshell binding is evaluated through two-photon laser scanning microscopy in Fig. 3. The figure shows phase-

contrast images overlaid with the two-photon images. The cells incubated with media only demonstrate no nanoshell signal. The HER2+ cell lines incubated with nanoshells each show nanoshell signal, while the HER2-cell line shows significantly less. The SK-BR-3 and BT474 AZ LR cell lines show the most nanoshell binding. The JIMT-1 cell line demonstrates less nanoshell binding than the SK-BR-3 and BT474 AZ LR cell lines, but greater nanoshell binding than the MCF10A cell line. There is some degree of binding seen with the MCF10A cell line, but this binding is still significantly less than the HER2+ breast cancer cells.

Nanoshell-mediated cell destruction of trastuzumab-resistant cell lines

Figure 4 shows the live/dead imaging and silver staining for the treatment and media control group of each cell line. None of the media alone groups show evidence of cell death on the live/dead images or evidence of nanoshell binding on the silver stain. The silver staining confirms that nanoshells are bound to each of the HER2+ cell lines (SK-BR-3, BT474 AZ LR, JIMT-1), with minimal nanoshell binding to the MCF10A cell line. The MCF10A-nanoshell group does not demonstrate localized area of cell death, while each of the HER2+ breast cancer-nanoshell groups show a clearly defined region of dead cells (red)

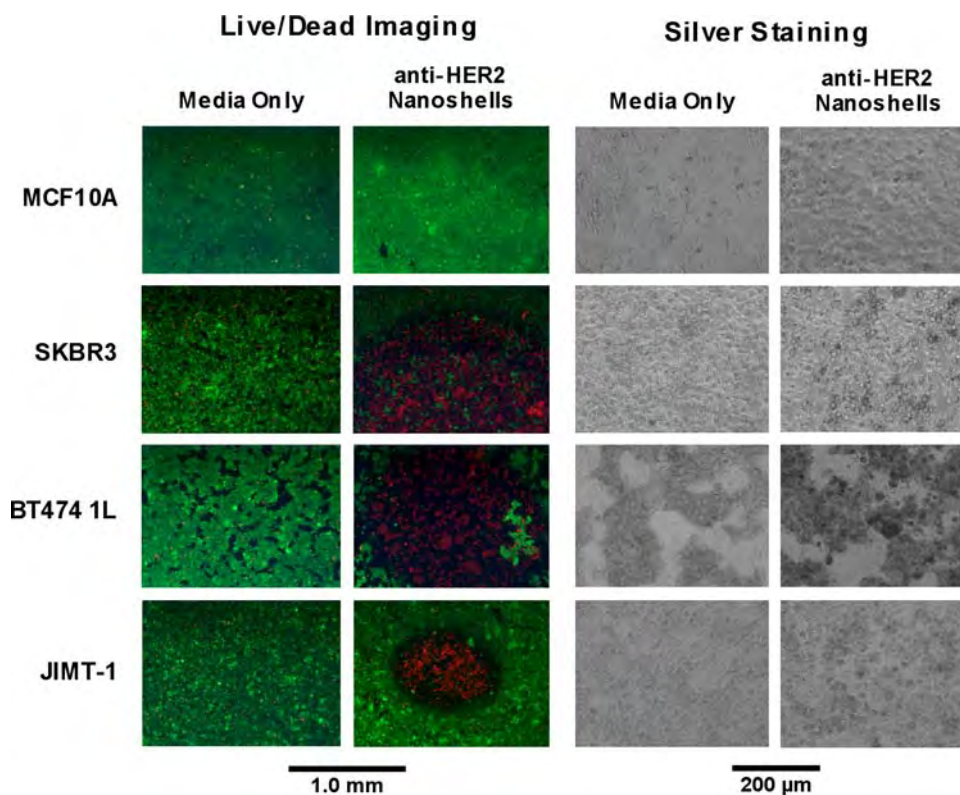
corresponding to the laser spot surrounded by non-irradiated, nanoshell-bound live cells (green).

Discussion

Anti-HER2 resistance continues to be a challenge for clinicians treating advanced cancers. Gold nanoparticle-mediated photothermal therapy could present new possibilities for cancers that are currently resistant to conventional chemotherapy and radiation treatments. The objective of this study was to demonstrate that immunoconjugated silica-gold nanoshells can effectively destroy both chemotherapy-sensitive and chemotherapy-resistant breast cancer cell lines. Two trastuzumab-resistant breast cancer cell lines were selected for testing, JIMT-1 and BT474 AZ LR. A trastuzumab-sensitive breast cancer cell line, SK-BR-3, and a HER2 negative normal epithelial cell line, MCF10A, were also chosen as positive and negative binding controls. Each of the HER2+ breast cancer cell lines selected was effectively ablated using nanoshell-mediated photothermal therapy. These results suggest gold nanoparticle-mediated photothermal therapy may have potential to be employed against chemotherapy-resistant breast cancers *in vivo*.

As the first step of this study, we evaluated nanoshell binding efficiency using two-photon laser scanning

Fig. 4 Photothermal therapy results. Live/dead imaging demonstrates cell ablation in HER2+ cell lines (SK-BR-3, JIMT-1, BT474 AZ LR) treated with anti-HER2 nanoshells and NIR laser irradiation. Silver staining shows nanoshell binding for each of the HER2+ cell lines



microscopy. Silica–gold nanoshells have demonstrated two-photon properties, and can be used to label HER2+ breast cancer cells in vitro [24, 25]. Nanoshell binding has also been demonstrated using darkfield microscopy [15] and optical coherence tomography [26], which depends on the enhanced scattering of the nanoshells for contrast. However, for future in vivo studies, two-photon luminescence may prove superior in bulk tissue to these scatter-based techniques. This is due to the improved signal to noise ratio of two-photon microscopy, as well as its demonstrated ability to more effectively investigate the nanoshell distribution within the tumor with the assistance of software [25]. In Fig. 3, we observe that the anti-HER2 conjugated silica–gold nanoshells bind specifically to trastuzumab-resistant HER2+ breast cancer cell lines, with very little binding to the normal breast epithelial cell line, MCF10A (Figs. 3, 4). The degree of nanoshell binding shown by both the two-photon and silver stain images seems to correlate with the HER2 antigen binding capacity of the breast cancer cell lines. The JIMT-1 cell line has the lowest anti-HER2 binding capacity of the three breast cancer lines studied. Nagy et al. found that only 20% of HER2 receptors are available for trastuzumab binding due to obstruction of the extracellular component of the HER2 receptor by MUC4 [9]. Despite this, anti-HER2 nanoshell binding is still clearly seen in both the two-photon and silver stain images, though to a lesser degree than the other two HER2+ lines. Importantly, this lesser degree of binding is still sufficient for the photothermal destruction of the JIMT-1 cells, while the action of trastuzumab is impaired against these cells [9]. In the case of the BT474 AZ LR cell line, the nanoshell binding is more than adequate to ensure cell death upon NIR laser irradiation. Photothermal therapy is also effective against the BT474 AZ LR cell line, while the action of both trastuzumab and lapatinib is impaired against these cells.

Using silica–gold nanoshells as a mediating absorptive agent for photothermal therapy has advantages over conventional hyperthermia treatments. In Fig. 4, the ablated areas (red) are surrounded by living, healthy cells (green), and cell lines with minimal or no nanoshell binding show no regions of cell death. Only HER2+ cells with bound nanoshells within the region of the laser spot are ablated. Targeting the gold nanoparticles with an antibody or peptide permits single cell specificity in vitro [27, 28]. This specificity is important during in vivo studies, when healthy tissues such as skin will be in the laser path to cancerous tissue. Because nanoshells efficiently absorb the irradiating laser energy and convert it to heat, the laser power requirements to induce cell death are lowered. In conventional hyperthermia treatments, this specificity is lacking, as the power of the irradiating energy source must be high enough to kill cells without the assistance of a

mediating agent. Thus, using nanoshells as part of photothermal therapy in vitro lowers the power requirements of the irradiating energy, as well as increasing the specificity of therapy for malignant cells.

Figure 4 does demonstrate some variation in the size of the ablated regions. This variation was seen consistently among several replicate experiments. These differences are likely due to variations in the laser intensity distribution, the degree of cell confluence, and density of HER2 receptors on the cell surfaces. In order for cell death to occur, a temperature of 70–80°C must be achieved for approximately 4 min [13]. The net temperature increase of the cells within the laser spot is dependent on a combination of variables, including: the absorptive cross-section of the silica–gold nanoshells, the physical distribution of the nanoshells among the cells, the intensity and duration of the laser illumination, and the heat transfer and dissipation properties of the cells and media [29]. Nonuniform laser intensity could lead to cells at the periphery of the spot receiving less laser power [30], resulting in the minimum temperature and duration needed for cell death not being achieved. However, the laser spot size, power, and duration were held consistent throughout each of the treatment groups and experiments, so it is unlikely that this is a large contributor. The nanoshell binding density could also be playing a significant role, and, based on the information in Figs. 2 and 3, is a likely contributor to the variation in ablated area size.

The low anti-HER2 binding capacity of the JIMT-1 cell line versus the higher binding capacities of the SK-BR-3 and BT474 AZ LR cell lines correlates with the small ablated area for the JIMT-1 cells and the larger ablated areas for the SK-BR-3 and BT474 AZ LR cells. This supports the nanoshell binding density being a major contributor to the variation in ablation size. However, although the SK-BR-3 cell line has a lower anti-HER2 binding capacity than the BT474 AZ LR cell line, the size of the ablated area for this cell line is larger. This could be due to several factors. Some of this variation may be due to the differences in how the SK-BR-3 and BT474 AZ LR cell lines tend to grow. The SK-BR-3 cells grow in a monolayer, while the BT474 AZ LR cell line tends to grow in conglomerates. These growth differences may have resulted in different heating profiles between the two cell lines, affecting the sizes of the ablated regions. Another possible contributing factor is differences in thermal sensitivity between the SK-BR-3 and BT474 AZ LR cell lines, which has been seen in response to conventional hyperthermia treatments in tumors resected from breast cancer patients [31]. Regardless of variation in the size of the ablated regions, each of the HER2+ breast cancer cell lines was successfully ablated using nanoshell-mediated photothermal therapy. Each of these variables (laser intensity profile,

nanoshell binding density, the tumor cell density/tumor shape, the thermal sensitivity of the tumor) will need to be considered in applying and optimizing nanoshell-mediated therapy to trastuzumab-resistant cancers in vivo.

The successful application of gold nanoshell-mediated photothermal therapy to trastuzumab-resistant breast cancer cells in vitro suggests a promising new approach for the treatment of advanced HER2+ breast cancers. By virtue of its physical means of destroying cancer, nanoshell-mediated thermal ablation of these types of cancer has an innate advantage over trastuzumab, lapatinib, and other antibody or small molecule-based therapies. Gold nanoparticle-mediated photothermal therapies also have demonstrated synergistic cell killing in combination with chemotherapy in vitro [32] and radiation in vivo [33], suggesting that the combination of conventional treatments and this technology could also be beneficial for cancer therapy. In vivo studies with xenografted trastuzumab-resistant breast cancers are currently underway to further confirm the efficacy and applicability of this nanotechnology to anti-HER2-resistant breast cancers.

Acknowledgments We would like to thank Wendy Schober at MDACC for performing the flow cytometry on each cell line. This study was supported by a Department of Defense Congressionally Directed Breast Cancer Research Program Era of Hope Scholar Award to Rebekah Drezek and Tse-Kuan Yu, the Center for Biological and Environmental Nanotechnology (EEC-0118007 and EEC-0647452), the NCI breast cancer SPORE P50 (CA58183), and the Nancy Owens Memorial Foundation (Y. Li). L. Carpin would also like to thank the Medical Scientist Training Program at Baylor College of Medicine for training support.

References

1. American Cancer Society: Breast Cancer Facts and Figures (2007–2008) In: breast cancer facts and figures 2007–2008. American Cancer Society, Atlanta
2. Nahta R, Yu D, Hung MC, Hortobagyi GN, Esteva FJ (2006) Mechanisms of disease: understanding resistance to HER2-targeted therapy in human breast cancer. *Nat Clin Pract* 3(5):269–280
3. Slamon DJ, Clark GM, Wong SG, Levin WJ, Ullrich A, McGuire WL (1987) Human breast cancer: correlation of relapse and survival with amplification of the HER-2/neu oncogene. *Science* 235(1):177–182
4. Cobleigh MA, Vogel CL, Tripathy D, Robert NJ, Scholl S, Fehrenbacher L, Wolter JM, Paton V, Shak S, Lieberman G et al (1999) Multinational study of the efficacy and safety of humanized anti-HER2 monoclonal antibody in women who have HER2-overexpressing metastatic breast cancer that has progressed after chemotherapy for metastatic disease. *J Clin Oncol* 17(9):2639–2648
5. Vogel CL, Cobleigh MA, Tripathy D, Gutheil JC, Harris LN, Fehrenbacher L, Slamon DJ, Murphy M, Novotny WF, Burchmore M et al (2002) Efficacy and safety of trastuzumab as a single agent in first-line treatment of HER2-overexpressing metastatic breast cancer. *J Clin Oncol* 20(3):719–726
6. Nahta R, Esteva FJ (2006) HER2 therapy: molecular mechanisms of trastuzumab resistance. *Breast Cancer Res* 8(6):215
7. Valabrega G, Montemurro F, Aglietta M (2007) Trastuzumab: mechanism of action, resistance and future perspectives in HER2-overexpressing breast cancer. *Ann Oncol* 18(6):977–984
8. Hirsch LR, Stafford RJ, Bankson JA, Sershen SR, Rivera B, Price RE, Hazle JD, Halas NJ, West JL (2003) Nanoshell-mediated near-infrared thermal therapy of tumors under magnetic resonance guidance. *Proc Natl Acad Sci USA* 100(23):13549–13554
9. Nagy P, Friedlander E, Tanner M, Kapanen AI, Carraway KL, Isola J, Jovin TM (2005) Decreased accessibility and lack of activation of ErbB2 in JIMT-1, a herceptin-resistant, MUC4-expressing breast cancer cell line. *Cancer Res* 65(2):473–482
10. Lu Y, Zi X, Zhao Y, Mascarenhas D, Pollak M (2001) Insulin-like growth factor-I receptor signaling and resistance to trastuzumab (Herceptin). *J Natl Cancer Inst* 93(24):1852–1857
11. Yakes FM, Chinratanalab W, Ritter CA, King W, Seelig S, Arteaga CL (2002) Herceptin-induced inhibition of phosphatidylinositol-3 kinase and Akt is required for antibody-mediated effects on p27, cyclin D1, and antitumor action. *Cancer Res* 62(14):4132–4141
12. Huang X, Qian W, El-Sayed IH, El-Sayed MA (2007) The potential use of the enhanced nonlinear properties of gold nanospheres in photothermal cancer therapy. *Lasers Surg Med* 39(9):747–753
13. Huang X, El-Sayed IH, Qian W, El-Sayed MA (2006) Cancer cell imaging and photothermal therapy in the near-infrared region by using gold nanorods. *J Am Chem Soc* 128(6):2115–2120
14. Skrabalak SE, Chen J, Au L, Lu X, Li X, Xia Y (2007) Gold nanocages for biomedical applications. *Adv Mater* 19(20):3177–3184
15. Loo C, Lin A, Hirsch L, Lee MH, Barton J, Halas N, West J, Drezek R (2004) Nanoshell-enabled photonics-based imaging and therapy of cancer. *Technol Cancer Res Treat* 3(1):33–40
16. Loo C, Lowery A, Halas N, West J, Drezek R (2005) Immunotargeted nanoshells for integrated cancer imaging and therapy. *Nano Lett* 5(4):709–711
17. Bernardi RJ, Lowery AR, Thompson PA, Blaney SM, West JL (2008) Immunonanoshells for targeted photothermal ablation in medulloblastoma and glioma: an in vitro evaluation using human cell lines. *J Neurooncol* 86(2):165–172
18. Gobin AM, Moon JJ, West JL (2008) EphrinA I-targeted nanoshells for photothermal ablation of prostate cancer cells. *Int J Nanomed* 3(3):351–358
19. Stern JM, Stanfield J, Lotan Y, Park S, Hsieh JT, Cadeddu JA (2007) Efficacy of laser-activated gold nanoshells in ablating prostate cancer cells in vitro. *J Endourol/Endourol Soc* 21(8):939–943
20. Elghanian R, Storhoff JJ, Mucic RC, Letsinger RL, Mirkin CA (1997) Selective colorimetric detection of polynucleotides based on the distance-dependent optical properties of gold nanoparticles. *Science* 277(5329):1078–1081
21. Bickford LR, Agollah G, Drezek R, Yu TK (2009) Silica-gold nanoshells as potential intraoperative molecular probes for HER2-overexpression in ex vivo breast tissue using near-infrared reflectance confocal microscopy. *Breast cancer research and treatment* [Epub ahead of print]
22. Oldenburg SJ, Averitt RD, Westcott SL, Halas NJ (1998) Nano-engineering of optical resonances. *Chem Phys Lett* 288(2–4):243–247
23. Stober W, Fink A, Bohn E (1968) Controlled growth of monodisperse silica spheres in micron size range. *J Colloid Interf Sci* 26(1):62–69
24. Bickford L, Sun J, Fu K, Lewinski N, Nammalvar V, Chang J, Drezek R (2008) Enhanced multi-spectral imaging of live breast

- cancer cells using immunotargeted gold nanoshells and two-photon excitation microscopy. *Nanotechnology* 19(31): 315102
25. Park J, Estrada A, Sharp K, Sang K, Schwartz JA, Smith DK, Coleman C, Payne JD, Korgel BA, Dunn AK et al (2008) Two-photon-induced photoluminescence imaging of tumors using near-infrared excited gold nanoshells. *Opt Express* 16(3):1590–1599
 26. Gobin AM, Lee MH, Halas NJ, James WD, Drezek RA, West JL (2007) Near-infrared resonant nanoshells for combined optical imaging and photothermal cancer therapy. *Nano Lett* 7(7):1929–1934
 27. Black KC, Kirkpatrick ND, Troutman TS, Xu L, Vagner J, Gillies RJ, Barton JK, Utzinger U, Romanowski M (2008) Gold nanorods targeted to delta opioid receptor: plasmon-resonant contrast and photothermal agents. *Mol Imaging* 7(1):50–57
 28. Tong L, Zhao Y, Huff TB, Hansen MN, Wei A, Cheng JX (2007) Gold nanorods mediate tumor cell death by compromising membrane integrity. *Adv Mater* 19:3136–3141
 29. Cheong SK, Krishnan S, Cho SH (2009) Modeling of plasmonic heating from individual gold nanoshells for near-infrared laser-induced thermal therapy. *Med Phys* 36(10):4664–4671
 30. de Lange DF, Hofman JT, Meijer J (2005) Influence of intensity distribution on the melt pool and clad shape for laser cladding. In: Third international WLT-conference on lasers in manufacturing: 2005; Munich, Germany
 31. Rofstad EK (1990) Heat sensitivity and thermotolerance in vitro of human breast carcinoma, malignant melanoma and squamous cell carcinoma of the head and neck. *Br J Cancer* 61(1):22–28
 32. Hauck TS, Jennings TL, Yatsenko T, Kumaradas JC, Chan WCW (2008) Enhancing the toxicity of cancer chemotherapeutics with gold nanorod hyperthermia. *Adv Mater* 20(20):3832–3838
 33. Diagaradjane P, Shetty A, Wang JC, Elliott AM, Schwartz J, Shentu S, Park HC, Deorukhkar A, Stafford RJ, Cho SH et al (2008) Modulation of in vivo tumor radiation response via gold nanoshell-mediated vascular-focused hyperthermia: characterizing an integrated antihypoxic and localized vascular disrupting targeting strategy. *Nano Lett* 8(5):1492–1500

Symmetry Breaking in Gold–Silica–Gold Multilayer Nanoshells

Ying Hu,[†] Sterling J. Noelck,[†] and Rebekah A. Drezek^{†,*}

[†]Department of Bioengineering and [‡]Department of Electrical and Computer Engineering, Rice University, Houston, Texas 77005

Up to date, symmetry breaking has been investigated in a variety of gold nanostructures from three-dimensional nanoeegs¹ and nanocups² to two-dimensional disk/ring,^{3,4} two-layer, and planar nanocavities.^{5,6} In nanoeegs, where the silica core is off-centered in a silica–gold core–shell nanoshell, both far-field and near-field properties have been studied as functions of the core offset.¹ It was found that a larger offset correlates with larger red shifts in the low-energy plasmon resonant peaks, a stronger near-field enhancement, and a larger absorption-to-scattering ratio at the dipole resonance.¹ The polarization of light only weakly affects the far-field spectrum.² However, in nanocups where the gold shell is partially opened up by the offsetting core, the far-field scattering spectrum strongly depends on polarization owing to its anisotropic geometry.⁷ As the core further protrudes from the shell, dipole modes gradually weaken and eventually vanish.¹

Studies of two-dimensional structures have revealed some interesting phenomena. In geometries with reduced symmetry, the highly damped multipolar modes are excited and interact with the dipole mode. Liu and co-workers demonstrated a carefully designed planar geometry in which the narrow quadrupole resonance of the nanobar/nanoslit dimer destructively interferes with the broad dipole mode of the nanobar/nanoslit monomer that is off-centered, leading to a narrow region where light transmission is significantly enhanced; in atomic physics, this is known as electromagnetically enhanced interference (EIT).^{5,6} Similarly, Hao *et al.* reported a nonconcentric ring/disk nanocavity in which the broad dipole mode both constructively and de-

ABSTRACT We present a computational study of the plasmonic properties of gold–silica–gold multilayer nanoshells with the core offset from the center. Symmetry breaking, due to the core offset, makes plasmon resonances that are dark in concentric geometries visible. Applying plasmon hybridization theory, we explain the origin of these resonances from the interactions of an admixture of both primitive and multipolar modes between the core and the shell. The interactions introduce a dipole moment into the higher order modes and significantly enhance their coupling efficiency to light. To elucidate the symmetry breaking effect, we link the geometrical asymmetry to the asymmetrical distribution of surface charges and demonstrate illustratively the diminishing multipolar characteristic and increasing dipolar characteristic of the higher order modes. The relative amplitudes of the modes are qualitatively related by visual examination of the dipolar component in the surface charge distributions. Using polarization-dependent surface charge plots, we illustrate two distinct mode configurations despite their spectral similarities. We further demonstrate a trend of increasing absorption relative to scattering as the resonant wavelength red shifts in response to a larger core offset.

KEYWORDS: plasmonics · multilayer nanoshells · symmetry breaking · plasmon hybridization · surface charge distribution

structively interferes with a sharp quadrupole mode. The interaction results in an asymmetrical sharp Fano-type resonance.^{3,4} Due to the sharp nature of the Fano resonance, symmetry-breaking geometries have been proposed for nanoscale optical sensing such as high figure-of-merit metamaterial sensors.⁵ It has also been found that offset geometries exhibit significantly larger local-field enhancement, making them promising for surface-enhanced spectroscopies.^{1–3}

Multilayer nanoshells (MNS) preserve three-dimensional spherical symmetry, as in nanoeegs, but they also exhibit symmetry-breaking patterns similar to ring/disk nanocavities. Theoretical investigations of concentric MNS have been previously reported using various Mie-based approaches.^{8–11} It has been found that the addition of a gold core to the gold shell splits the low-energy plasmon resonance of a conventional silica–gold core–shell nanoshell (CNS) into a high-energy

*Address correspondence to drezek@rice.edu.

Received for review December 1, 2009 and accepted February 02, 2010.

Published online February 10, 2010. 10.1021/nn901743m

© 2010 American Chemical Society

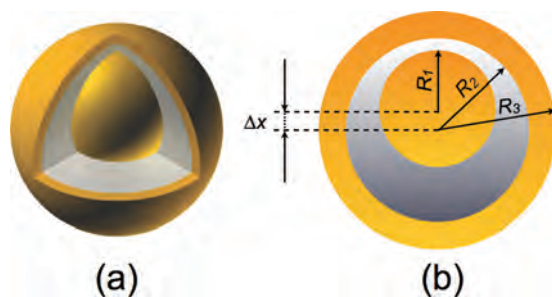


Figure 1. (a) Three-dimensional illustration of a gold-silica-gold multilayer nanoshell with an offset core. (b) Dimensions of an $R_1/R_2/R_3$ gold-silica-gold multilayer nanoshell with core offset Δx .

antibonding mode and a low-energy bonding mode that can be tuned from the visible region into the infrared. The red shift of this mode correlates with intermediate silica layer thickness, which determines the strength of coupling between the core mode and the CNS mode. As the mode red shifts, the MNS becomes relatively more absorbing than scattering at the bonding-mode resonance.¹⁰ An experimental study of MNS has also been published. Xia and co-workers reported the chemical synthesis of sub-100 nm multilayer nanoshells.¹² The silica coating on gold was achieved using a modified Stöber method.^{13–16} The final gold layer was coated in a way similar to synthesizing silica-gold core-shell nanoshells.^{17,18}

Here we use a computational model to investigate MNS with an offset geometry: the inner gold core is moved away from the center but does not touch the gold shell, as illustrated in Figure 1a. The MNS dimensions are denoted by the radius of each layer, R_1 , R_2 , and R_3 , as well as the core offset, Δx , shown in Figure 1b. We apply plasmon hybridization theory to obtain insight into spectral properties of the MNS. This theory is analogous to molecular orbital theory and describes how the fixed-frequency plasmons of elementary nanostructures hybridize to create more complicated resonances. It has been used to explain the plasmonic properties of structures ranging from concentric nanoshells^{19,20} to nanorice^{21–24} to nanosphere trimers^{25,26} and quadrumers.²⁵ Some interesting examples of plasmon hybridization applied to nonsymmetrical structures include analyzing the aforementioned nanocups^{1,2,7} and nonconcentric ring/disk structures.^{3,4}

The far-field properties of MNS were simulated using a finite-element method (FEM) package: COMSOL Multiphysics v3.5a with the RF module. Because the dimensions of the gold core and shell remain unaltered as the location of the core changes, the offset process itself does not require size correction for the dielectric function of gold due to intrinsic effects. It should also be noted that this work does not focus on the spectral width of plasmon resonances, which can be consider-

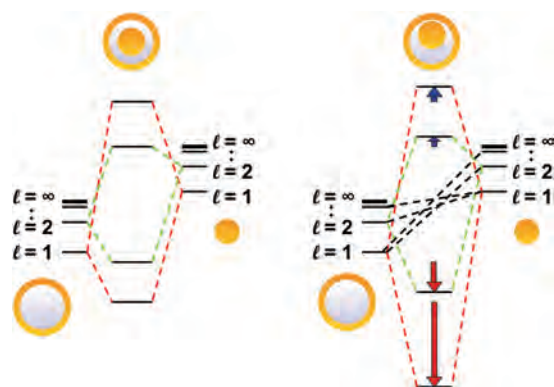


Figure 2. Hybridization diagrams of MNS with concentric (left) and offset (right) geometries. The left panel illustrates the plasmon hybridization diagram for a concentric MNS with interaction between modes having the same angular momentum (energy increases from bottom to top). The right panel displays the nonconcentric MNS case with black lines showing additional interactions and arrows showing the relative red shift and blue shift (not to scale). Only dipole and quadrupolar interactions are shown for clarity.

ably broadened by the surface scattering of electrons in nanostructures.^{27–30}

RESULTS AND DISCUSSION

Plasmon Hybridization. An MNS can be modeled as a hybrid between a silica-gold core-shell nanoshell and a solid gold core. We apply plasmon hybridization to explain the optical properties of MNS using these two basic nanostructures. The hybridization diagrams in Figure 2 show, for both the concentric and offset MNS, the interactions between the hybridized modes of the nanoshell and the spherical plasmon modes of the core. For clarity, only the dipolar and quadrupolar interactions are shown. The antibonding modes from the nanoshell are not shown because they are higher energy and have only very weak interactions with the core mode. The left panel of Figure 2 shows the hybridization diagram for the concentric MNS where the modes of different angular momenta are forbidden from interacting. Like the hybridization between the inner and outer layers of a nanoshell, there are two modes for each interaction: a low-energy bonding mode and a higher energy antibonding mode. This can be seen in the left panel of Figure 2 for the dipole-dipole ($l = 1$) and quadrupole-quadrupole ($l = 2$) interaction. For the nonconcentric case, the selection rules for interaction are relaxed, allowing modes of different orders to mix. As depicted in the right panel of Figure 2, the dipole mode ($l = 1$) of the core can now interact with not only the dipole mode ($l = 1$) of the shell but also the quadrupole and higher order modes ($l = 2, 3$, etc.) of the shell. Additionally, the quadrupole ($l = 2$) of the shell can now interact with the dipole ($l = 1$) of the core, bringing in the dipole moment into the quadrupole mode.

The hybridization between different modes on the core and the shell also results in red shifts of the hybrid-

ized bonding modes of MNS. The lower order modes are red-shifted as they become repelled by the interaction with higher order modes. As shown in the right panel of Figure 2, this yields a shift for the predominately dipole–dipole hybridized modes that is larger than for the quadrupole–quadrupole hybridized modes, and so on. In addition to a red shift of the bonding modes, the antibonding hybridized modes are slightly blue-shifted. This leads to a very asymmetrical splitting of the hybridized energy modes. Such asymmetrical splitting is seen in other nanostructures as the symmetry is broken,^{2,4,31} as well as in nanoparticle dimers.^{32,33} The degree of the shift is determined by the strength of the interactions between the different modes. As the gold core is offset more and approaches the gold nanoshell, the plasmons of the core interact more strongly with plasmons of the shell. These increasing interactions lead to stronger mixing between the different modes, creating a greater shift from the concentric MNS interactions.

Symmetry Breaking in MNS with Different Geometries. As seen in the work on concentric multilayer nanoshells, changing the ratio of the core, silica layer, and the outer layer allows tuning of the plasmon resonance.¹⁰ This same effect is seen in offset multilayer nanoshells, as well. Figures 3 and 4 show the extinction spectra of the offset MNS with two different $R_1/R_2/R_3$ ratios as well as different outer radii R_3 . Figure 3 shows R10/15/25 nm MNS in water with various core offsets. The black stars from the Mie calculation agree very well with the black curve from the FEM calculation of a concentric geometry. Two distinct plasmon resonant peaks can be observed in the concentric spectrum. The high-energy peak around 530 nm is the antibonding mode of the dipole–dipole interaction between the shell and the core along with other higher order modes. The interband transitions of gold lead to a pronounced broadening and damping of all modes in this region.^{34–36} The low-energy peak at 643 nm is the bonding mode of the dipolar interaction. Quadrupole modes are not excited as the particle lies in the quasi-static region. When the symmetry is reduced and the mode selection rule for hybridization is relaxed, modes of different angular momenta start to interact.^{1,2,31} Among the offset spectra, one can immediately observe a red shift of the dipolar bonding mode. The fact that the dipole of the core is allowed to interact with the quadrupole of the shell and *vice versa* shifts the bonding mode to a lower energy. The blue shift of the antibonding mode, however, is too small to be visualized in the spectrum. In addition to the red shift of the bonding modes and blue shift of the antibonding modes, hybridization results in the appearance of dark modes that were only weakly excited or not excited at all in the concentric MNS. For instance, one can observe the emergence of a new peak at about 592 nm. This peak is likely to be the bonding mode of the quadrupole–quadrupole interaction between the

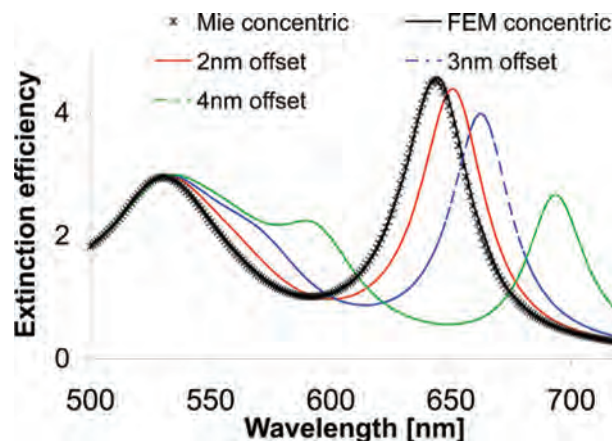


Figure 3. Extinction spectra of R10/15/25 nm MNS in water with various core offsets. Core offsets in y; incident light linearly polarized in x and propagates in z.

shell and the core (noted by $l = 2$ in the hybridization diagram). This mode can be directly excited because the interaction between the quadrupole and dipole modes introduces a small overall dipole moment in the plasmon. This mode is not excitable in the concentric case because of the lack of the dipole moment in the quadrupole–quadrupole interaction.

Although interesting in nature, the quadrupole peak is still not very well-defined at the largest offset we calculated. In Figure 4, we demonstrate the spectra of a larger MNS: R30/40/50 nm in water with a different $R_1/R_2/R_3$ ratio (3/4/5 instead of 2/3/5). The particle lies outside the quasistatic region and can provide opportunities to observe sharp higher order modes. As shown in Figure 4, good agreement was obtained between Mie and FEM calculations on the concentric geometry. The relatively large size of the MNS and limitations from the meshing and scattering boundary condition in COMSOL v3.5a may account for the $\sim 6\%$ discrepancy on the peak intensity at 890 nm.³⁷ For clarity, each resonant peak is labeled with a numerical value associated with its mode (*i.e.*, 1 for dipole, 2 for quadrupole, etc.), followed by a letter denoting the core offset of that spectrum.

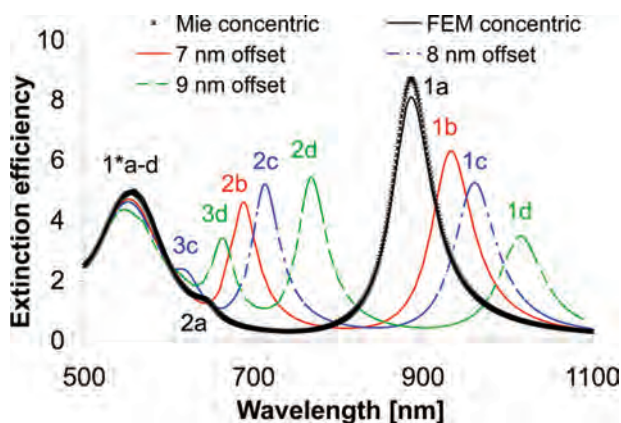


Figure 4. Extinction spectra of R30/40/50 nm MNS in water with various core offsets. Core offsets in y; incident light linearly polarized in x and propagates in z.

In the concentric spectrum, in addition to the dipolar modes at 1a and 1*a, a slight quadrupolar peak can be observed at 2a. The excitation of this mode is attributed to the retardation effect as the particle size is comparable to the excitation wavelength. Its small amplitude reflects a lack of the dipole moment. More specifically, the amplitude of the extinction peak is directly proportional to the square of the dipole moment. When the symmetry is reduced, as shown in the 7 nm offset spectrum (red), the dipolar bonding mode is red-shifted from 886 to 934 nm (1a to 1b) and the quadrupolar bonding mode is shifted from ~644 to 688 nm (2a to 2b). While the peak intensity of 1b is decreased, that of 2b is significantly enhanced. The enhancement at 2b is due to the dipole–quadrupole interaction that adds a dipolar component into the quadrupole mode. Likewise, the interaction between the dipole of the core/shell and higher order modes of the core/shell introduces dark characteristics of the multipolar modes into 1b and causes its amplitude to decrease.

From a macroscopic perspective, the *f-sum law* can be used to interpret the relative change of the peak amplitude at each plasmon mode.^{38,39} In the MNS system, where the number of oscillating electrons is fixed, the convolution of the amplitudes of plasmon resonances with their energy levels remains a constant. This does not, however, indicate that an increase in one peak necessarily causes a decrease in another peak. In the 7 nm offset spectrum, nevertheless, the significant gain at the high-energy quadrupolar mode demands that the dipolar mode be both down shifted in energy and decreased in amplitude.

As the core continuously moves away from the center, more modes that are completely dark in the concentric spectrum start to emerge. In the 8 nm (blue) and 9 nm (green) offset spectra, the emergence of the 3c mode at ~620 nm and the 3d mode at 664 nm is the octupole mode excited with added dipole components. As previously described by the *f-sum law*, the introduction of this new octupole mode results in a decrease in amplitude of the dipole mode at 1c and 1d.

Surface Charge Distribution and the Polarization Effect. While hybridization theory qualitatively explains the plasmon resonances of MNS, it does not provide information regarding charge distributions on metal–dielectric interfaces at each resonant mode. Furthermore, it does not describe the relative amplitude of each peak nor the polarization effect on the spectrum. Therefore, we supplement the hybridization analysis with surface charge distributions at the outer and inner layers of the gold shell as well as the surface of the gold core at resonant wavelengths. We examine both spectral properties and charge distributions of the MNS when the incident light is axially polarized with respect to the core offset and when it is transversely polarized.

Figure 5 shows the extinction spectra of the R30/40/50 nm MNS with a 9 nm offset core at two different

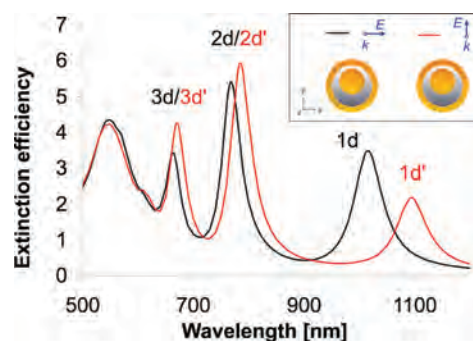


Figure 5. Extinction spectrum of the R30/40/50 nm MNS in water with 9 nm core offset. Black, incident light is transversely polarized with respect to the offset; red, incident light is axially polarized along the offset.

polarizations. The dipole, quadrupole, and octupole resonances can be clearly recognized, as described in previous sections. To facilitate the analysis, we denote these modes in the following fashion: dipole modes 1d (transverse) and 1d' (axial), quadrupole modes 2d (transverse) and 2d' (axial), and octupole modes 3d (transverse) and 3d' (axial). One can observe that the two spectra have very similar shapes, indicating minimal impact from polarization. It is worth noting that reported in the literature are three-dimensional nanoparticles whose plasmon resonances do not largely depend on the polarization, such as nanoeggs,² and nanoparticles whose spectra bear distinct polarization-dependent characteristics, such as nanocup.⁷ We conjecture that, since the offset MNS bear more resemblance to the nanoegg structure, the spectra should be largely polarization independent. One can observe in the axial spectrum slight red shifts in the bonding modes: from 1016 to 1094 nm for the dipole mode, 768 to 785 nm for the quadrupole mode, and 664 to 670 nm for the octupole mode. The red shift implies a stronger interaction between modes with different angular momenta when the light is axially polarized along the small gap between the core and the shell. One can also observe that 1d' has the largest red shift, whereas 3d' has the least. This is in agreement with the plasmon hybridization theory shown in Figure 2. In addition, the quadrupole and octupole peaks in the axially polarized spectrum (2d' and 3d') appear to be higher than those in the transversely polarized spectrum (2d and 3d), possibly owing to the stronger interaction. In both spectra, the quadrupole peaks (2d and 2d') appear to be higher than the octupole peaks (3d and 3d'). We will now explore these observations from the surface charge perspective. To calculate the surface charge, Gauss's law was applied to metal–dielectric interfaces. The phase of the solution was swept to find the correct distribution that corresponds to the maximal surface charge density. The extinction spectrum was calculated for the geometry in which the core offset and light polarization were (1) in orthogonal directions (transverse) and (2) along the same direction (axial).

Figure 6 shows the charge distribution on metal–dielectric interfaces for plasmon modes in the transverse spectrum. Side and top views (left and right panel) are provided. The color scales (not shown) on each surface are different for better illustration. Three relevant observations can be made. First, the distributions at 3d, 2d, and 1d resemble octupole, quadrupole, and dipole-like characteristics, respectively. Opposite charges are found on the surface along the E field direction in which light is polarized. At each resonance, the charge distribution exhibits an alternating half-ring shape stacked from the top to the bottom of the particle. The pattern is consistent with the predictions we made using plasmon hybridization theory. Second, one observes that the charge polarity is the same along the inner and outer surfaces of the gold shell. This corresponds to the bonding-mode configuration of the shell and indicates that the core is, in fact, interacting with the bonding mode of the shell. Further, the charge polarity on the inner core is oppositely aligned with the outer shell. This also corresponds to the low-energy configuration (bonding) of the MNS and indicates that the plasmon resonance is the low-energy bonding mode from the core–shell interaction. Lastly, the octupole, quadrupole, and dipole distributions appear spatially distorted. The nature of the spatial asymmetry indicates that the hybridized modes are composed of a mixture of modes with different angular momenta. For instance, a perfect quadrupole mode would appear evenly and symmetrically distributed along each quadrant of the spherical surface. The fact that the distribution is skewed, as can be seen in the left panel of Figure 6, is caused by the admixture of a dipole component polarized along the horizontal direction. Since the plasmon resonant peak amplitude is directly proportional to the square of the dipole moment, the quadrupole and octupole modes are enhanced due to the introduction of the dipole interaction and the added dipole components, whereas the dipole mode will have a lower peak owing to the interaction with the multipolar modes and a reduction of the dipole component. Additionally, the degree of asymmetry of the charge distributions for the multipolar modes directly implies the amount of the dipole moment that has been added to the mode. The 2d mode appears to be more asymmetrical in a quadrupole sense than 3d in an octupole sense, suggesting that 2d has a larger dipole moment. This is better revealed in the spectrum in Figure 5, where 2d has a higher amplitude than 3d.

When the incident light is axially polarized, the surface charge distributions exhibit distinct characteristics despite spectral similarities to the transverse polarization case. As shown in the right

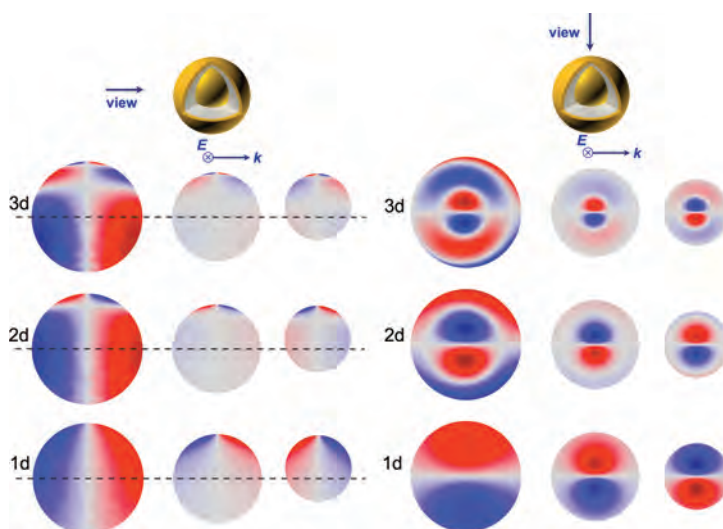


Figure 6. Side (left) and top (right) views of the surface charge plot of R30/40/50 nm MNS with 9 nm core offset at various hybridized plasmon peaks as the incident light is transversely polarized with respect to the offset. The three columns correspond to the outer gold shell (left), inner gold shell (middle), and inner gold core (right) layers. Red, positive charges; blue, negative charges. Horizontal dashed lines in the left panel mark the center location with respect to the core offset.

panel of Figure 7, the octupole and quadrupole distributions appear as whole rings instead of half rings across the entire particle. A larger dipole moment can be recognized in 3d' and 2d' as the charge distributions become more dipole-like. Meanwhile, the dipolar distributions in 1d' also appear distorted, indicating a large multipolar interaction, which attenuates and red shifts the resonant peak. Because the overall degree of asymmetry is larger in Figure 7 than in Figure 6, we conclude that the mode hybridization due to symmetry breaking is stronger when the light is axially polarized. This explains the overall red shift from 1d, 2d, and 3d to

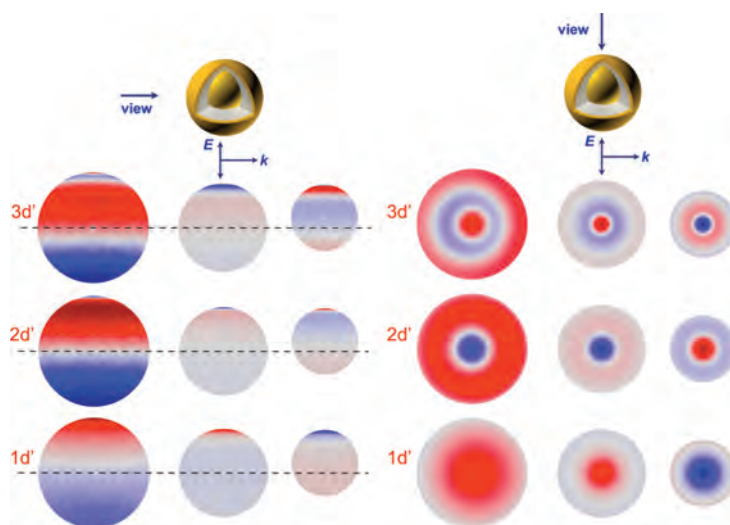


Figure 7. Side (left) and top (right) views of the surface charge plot of R30/40/50 nm MNS with 9 nm core offset at various hybridized plasmon peaks as the incident light is axially polarized along the offset. The three columns correspond to the outer gold shell (left), inner gold shell (middle), and inner gold core (right) surfaces. Red, positive charges; blue, negative charges. Horizontal dashed lines in the left panel mark the center location with respect to the core offset.

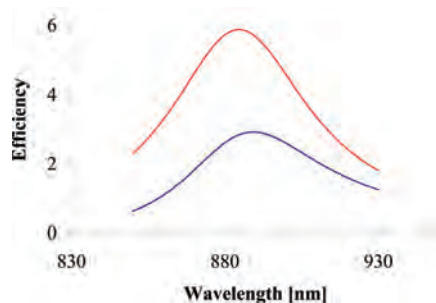


Figure 8. Mie-based calculation of the absorption (red) and scattering (blue) spectra of the concentric R30/40/50 nm MNS in water near the dipolar resonance.

1d', 2d', and 3d' and also the higher amplitudes at 2d', 3d' versus 2d, 3d and the lower amplitude at 1d' versus 1d, as previously described. It is worth noting that, due to the relatively large size of the particle (100 nm), the retardation from the propagating electromagnetic wave comes into play. For instance, in the right panels of Figures 6 and 7, the left–right asymmetry of the charge distribution for the octupole modes reveals this retardation effect. Waves travel in slightly different phase across the particle along the direction of the propagation (indicated by the k vector), which yields a slightly asymmetric charge distribution.

When MNS are excited by circularly polarized light (see Supporting Information), the surface charge distribution is a hybrid between the two types described above. The distributions not only appear distorted along the direction of the core offset but also become skewed around the spherical surface. The basic analysis, however, falls in the discussions for the axial and transverse polarizations.

Absorption Relative to Scattering. In concentric MNS, an increase of the gold core in an otherwise fixed geometry red shifts the dipolar bonding mode and renders the particle more absorbing than scattering at the plasmon resonance.¹⁰ It is thus of interest to investigate how the absorption of MNS changes with respect to scattering as a function of the core offset. We chose to focus on the dipolar and quadrupolar peaks and compare the absorption and scattering components of overall extinction. It is important to note that the wavelengths of peak values for absorption and scattering are slightly offset from each other. This is manifested not just in the FEM calculations of offset geometries but also in the Mie-based calculations of concentric geometries. The R30/40/50 nm MNS with a 9 nm offset and excited by transversely polarized light has an extinction peak at 886 nm, while the absorption peak is at 885 nm and the scattering peak at 889 nm. The offset is noticeable in Figure 8. The offset value, however, is small enough so the actual scattering and absorption values do not change very much. For consistency, we used the absorption and scattering values at the peak extinction wavelength for the comparisons in Figure 9a,b.

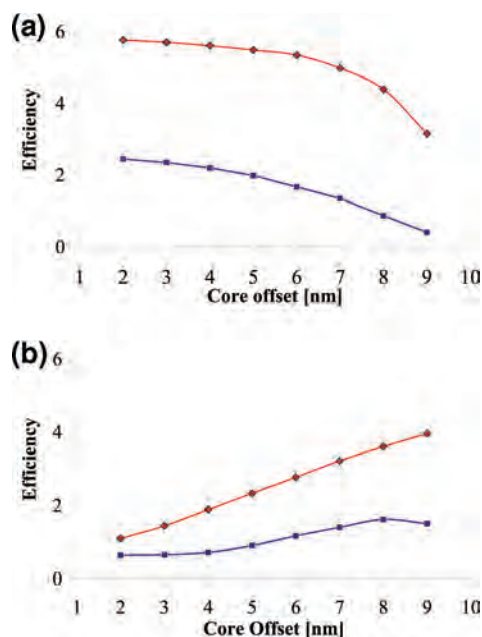


Figure 9. FEM calculation of the absorption (red) and scattering (blue) efficiency of the R30/40/50 nm MNS with a variable core offset in water (a) at the dipolar resonance and (b) at the quadrupolar resonance. Incident light transversely polarized.

From Figure 9a, it is clear that both scattering and absorption decrease with increasing offset, and the particle becomes more absorbing relative to scattering at the dipole peak. The scattering component steadily decreases and becomes almost insignificant at large offsets. The quadrupolar peak, shown in Figure 9b, is more complicated as the scattering first increases and then decreases after the 8 nm offset. Although with the decreasing scattering, the overall extinction continues to increase due to the rapidly growing absorption. The stronger absorption of the metal is mainly caused by a larger field confinement within a smaller volume (*i.e.*, the reducing gap between the core and the shell). These general trends are also seen in a R20/30/50 nm MNS (see Supporting Information). Overall, our results show a general trend toward a larger absorption component in the extinction peak as the core offset increases.

CONCLUSION

In this paper, we used plasmon hybridization theory and demonstrated that an offset of the core in an MNS allows interactions between plasmon resonances of different angular momenta. The mixing of modes allowed by the broken symmetry introduces a dipolar characteristic into higher order multipolar modes and makes them visible in the extinction spectra. We presented qualitatively in a hybridization diagram and quantitatively in the FEM calculations red shifts of the bonding plasmon modes as well as the emergence of the multipolar modes in the offset MNS. While polariza-

tion has little effect on the extinction spectra, we demonstrated that different polarizations create distinctly different surface charge distributions. We decomposed the extinction spectra into scattering and absorption and found that MNS tend to have a larger absorption component relative to scattering as the core offset increases. We postulate that offset MNS with larger dimensions will exhibit more interesting multiwavelength

plasmon resonances that are associated with even higher order modes. Assuming methods for large-scale synthesis can be developed, such particles may become valuable for multiplexed imaging. The distinctive spectral properties of MNS and their sensitivity to the core offset can also be harnessed to provide proof-of-concept studies for tracking intracellular movements of vessels and capsules that contain gold nanoparticles.

METHODS

For the FEM simulations, gold properties were obtained from Johnson and Christy.⁴⁰ The dielectric constant of silica was set to 2.04, and that for water to 1.33. The surrounding medium of MNS was water. Simulations were performed in COMSOL Multiphysics v3.5a. The simulation space and perfectly matched layer thickness were adjusted until agreement was obtained between the FEM and Mie-based calculations.¹⁰

For optical spectra, the scattering efficiency was calculated by integrating the normalized E field around a far-field transform boundary enclosing the MNS. The absorption efficiency was calculated by summing time-average resistive heating on the inner gold core and other gold shell. For surface charge plots, Gauss's law was applied:

$$\epsilon_0 \iint \vec{E} \cdot \vec{n} dS = \iint \sigma dS$$

The gradient operation was realized by implementing the *up* and *down* operators to the metal–dielectric interfaces in COMSOL.

Mie calculations were implemented in an in-house Matlab code written for simulating light scattering from concentric spheres with arbitrary number of layers.¹⁰ The dielectric function of gold was kept the same as the one used in FEM calculations, so were other parameters such as the refractive index of silica and water. The Mie code has been previously validated against literature results.^{10,41}

Acknowledgment. The authors thank P. Nordlander for insightful discussions on plasmon hybridization, and H. Khakestar for assistance with the COMSOL simulations, both from the Physics Department at Rice University. This work was financially supported by the Welch Foundation Grant C-1598, DoD CDMRP W81XWH-07-1-0428, the Gulf Coast Center for Computational Cancer Research, and the Center for Biological and Environmental Nanotechnology NSF EEC-0118007 and EEC-0647452. Y.H. is supported by the DoE CSGF program. S.J.N. is supported by the NSF IGERT fellowship program. The computational work was supported by the Shared University Grid at Rice University funded by NSF Grant EIA-0216467.

Supporting Information Available: Surface charge distributions from circularly polarized light and absorption vs scattering for R20/30/50 nm MNS. This material is available free of charge via the Internet at <http://pubs.acs.org>.

REFERENCES AND NOTES

- Knight, M. W.; Halas, N. J. Nanoshells to Nanoeggs to Nanocups: Optical Properties of Reduced Symmetry Core–Shell Nanoparticles Beyond the Quasistatic Limit. *New J. Phys.* **2008**, *10*, 105006.
- Wang, H.; Wu, Y. P.; Lassiter, B.; Nehl, C. L.; Hafner, J. H.; Nordlander, P.; Halas, N. J. Symmetry Breaking in Individual Plasmonic Nanoparticles. *Proc. Natl. Acad. Sci. U.S.A.* **2006**, *103*, 10856–10860.
- Hao, F.; Nordlander, P.; Sonnefraud, Y.; Van Dorpe, P.; Maier, S. A. Tunability of Subradiant Dipolar and Fano-Type Plasmon Resonances in Metallic Ring/Disk Cavities: Implications for Nanoscale Optical Sensing. *ACS Nano* **2009**, *3*, 643–652.
- Hao, F.; Sonnefraud, Y.; Van Dorpe, P.; Maier, S. A.; Halas, N. J.; Nordlander, P. Symmetry Breaking in Plasmonic Nanocavities: Subradiant LSPR Sensing and a Tunable Fano Resonance. *Nano Lett.* **2008**, *8*, 3983–3988.
- Liu, N.; Weiss, T.; Mesch, M.; Langguth, L.; Eigenthaler, U.; Hirscher, M.; Sonnefraud, Y.; Giessen, H. Planar Metamaterial Analogue of Electromagnetically Induced Transparency for Plasmonic Sensing. *Nano Lett.* **2009**, DOI: 10.1021/nl902621d.
- Liu, N.; Langguth, L.; Weiss, T.; Kastel, J.; Fleischhauer, M.; Pfau, T.; Giessen, H. Plasmonic Analogue of Electromagnetically Induced Transparency at the Drude Damping Limit. *Nat. Mater.* **2009**, *8*, 758–762.
- Lassiter, J. B.; Knight, M. W.; Mirin, N. A.; Halas, N. J. Reshaping the Plasmonic Properties of an Individual Nanoparticle. *Nano Lett.* **2009**, *9*, 4326–4332.
- Chen, K.; Liu, Y.; Ameer, G.; Backman, V. Optimal Design of Structured Nanospheres for Ultrasharp Light-Scattering Resonances as Molecular Imaging Multilabels. *J. Biomed. Opt.* **2005**, *10*, 024005.
- Khlebtsov, B.; Khlebtsov, N. Ultrasharp Light-Scattering Resonances of Structured Nanospheres: Effects of Size-Dependent Dielectric Functions. *J. Biomed. Opt.* **2006**, *11*, 044002.
- Hu, Y.; Fleming, R. C.; Drezek, R. A. Optical Properties of Gold–Silica–Gold Multilayer Nanoshells. *Opt. Express* **2008**, *16*, 19579–19591.
- Wu, D. J.; Liu, X. J. Tunable Near-Infrared Optical Properties of Three-Layered Gold–Silica–Gold Nanoparticles. *Appl. Phys. B* **2009**, *97*, 193–197.
- Xia, X. H.; Liu, Y.; Backman, V.; Ameer, G. A. Engineering Sub-100 nm Multi-layer Nanoshells. *Nanotechnology* **2006**, *17*, 5435–5440.
- Graf, C.; Vossen, D. L. J.; Imhof, A.; van Blaaderen, A. A General Method to Coat Colloidal Particles with Silica. *Langmuir* **2003**, *19*, 6693–6700.
- Kobayashi, Y.; Katakami, H.; Mine, E.; Nagao, D.; Konno, M.; Liz-Marzan, L. M. Silica Coating of Silver Nanoparticles Using a Modified Stöber Method. *J. Colloid Interface Sci.* **2005**, *283*, 392–396.
- Lee, H. B.; Yoo, Y. M.; Han, Y. H. Characteristic Optical Properties and Synthesis of Gold–Silica Core–Shell Colloids. *Scripta Mater.* **2006**, *55*, 1127–1129.
- Liz-Marzan, L. M.; Giersig, M.; Mulvaney, P. Synthesis of Nanosized Gold–Silica Core–Shell Particles. *Langmuir* **1996**, *12*, 4329–4335.
- Westcott, S. L.; Oldenburg, S. J.; Lee, T. R.; Halas, N. J. Formation and Adsorption of Clusters of Gold Nanoparticles onto Functionalized Silica Nanoparticle Surfaces. *Langmuir* **1998**, *14*, 5396–5401.
- Oldenburg, S. J.; Averitt, R. D.; Westcott, S. L.; Halas, N. J. Nanoengineering of Optical Resonances. *Chem. Phys. Lett.* **1998**, *288*, 243–247.
- Prodan, E.; Radloff, C.; Halas, N. J.; Nordlander, P. A Hybridization Model for the Plasmon Response of Complex Nanostructures. *Science* **2003**, *302*, 419–422.
- Radloff, C.; Halas, N. J. Plasmonic Properties of Concentric Nanoshells. *Nano Lett.* **2004**, *4*, 1323–1327.
- Sealy, C. Nanorice Combines Best of Both Worlds. *Nano Today* **2006**, *1*, 13.

22. Srivastava, D.; Lee, I. Nanorice and Nanospars from Polymer Nanospheres. *Adv. Mater.* **2006**, *18*, 2471–2475.
23. Wang, H.; Brandl, D. W.; Le, F.; Nordlander, P.; Halas, N. J. Nanorice: A Hybrid Plasmonic Nanostructure. *Nano Lett.* **2006**, *6*, 827–832.
24. Wiley, B. J.; Chen, Y. C.; McLellan, J. M.; Xiong, Y. J.; Li, Z. Y.; Ginger, D.; Xia, Y. N. Synthesis and Optical Properties of Silver Nanobars and Nanorice. *Nano Lett.* **2007**, *7*, 1032–1036.
25. Brandl, D. W.; Mirin, N. A.; Nordlander, P. Plasmon Modes of Nanosphere Trimers and Quadrumers. *J. Phys. Chem. B* **2006**, *110*, 12302–12310.
26. Jain, P. K.; El-Sayed, M. A. Surface Plasmon Coupling and Its Universal Size Scaling in Metal Nanostructures of Complex Geometry: Elongated Particle Pairs and Nanosphere Trimers. *J. Phys. Chem. C* **2008**, *112*, 4954–4960.
27. Berciaud, S.; Cognet, L.; Tamarat, P.; Lounis, B. Observation of Intrinsic Size Effects in the Optical Response of Individual Gold Nanoparticles. *Nano Lett.* **2005**, *5*, 515–518.
28. Kreibig, U.; Vollmer, M. *Optical Properties of Metal Clusters*; Springer: New York, 1995.
29. Moroz, A. Electron Mean Free Path in a Spherical Shell Geometry. *J. Phys. Chem. C* **2008**, *112*, 10641–10652.
30. Nehl, C. L.; Grady, N. K.; Goodrich, G. P.; Tam, F.; Halas, N. J.; Hafner, J. H. Scattering Spectra of Single Gold Nanoshells. *Nano Lett.* **2004**, *4*, 2355–2359.
31. Wu, Y. P.; Nordlander, P. Plasmon Hybridization in Nanoshells with a Nonconcentric Core. *J. Chem. Phys.* **2006**, *125*, 124708.
32. Lassiter, J. B.; Aizpurua, J.; Hernandez, L. I.; Brandl, D. W.; Romero, I.; Lal, S.; Hafner, J. H.; Nordlander, P.; Halas, N. J. Close Encounters between Two Nanoshells. *Nano Lett.* **2008**, *8*, 1212–1218.
33. Nordlander, P.; Oubre, C.; Prodan, E.; Li, K.; Stockman, M. I. Plasmon Hybridization in Nanoparticle Dimers. *Nano Lett.* **2004**, *4*, 899–903.
34. Hao, F.; Nordlander, P. Efficient Dielectric Function for FDTD Simulation of the Optical Properties of Silver and Gold Nanoparticles. *Chem. Phys. Lett.* **2007**, *446*, 115–118.
35. Perner, M.; Bost, P.; Lemmer, U.; vonPlessen, G.; Feldmann, J.; Becker, U.; Mennig, M.; Schmitt, M.; Schmidt, H. Optically Induced Damping of the Surface Plasmon Resonance in Gold Colloids. *Phys. Rev. Lett.* **1997**, *78*, 2192–2195.
36. Pinchuk, A.; Kreibig, U.; Hilger, A. Optical Properties of Metallic Nanoparticles: Influence of Interface Effects and Interband Transitions. *Surf. Sci.* **2004**, *557*, 269–280.
37. Khoury, C. G.; Norton, S. J.; Vo-Dinh, T. Plasmonics of 3-D Nanoshell Dimers Using Multipole Expansion and Finite Element Method. *ACS Nano* **2009**, *3*, 2776–2788.
38. Nozieres, P.; Pines, D. Electron Interaction in Solids—General Formulation. *Phys. Rev.* **1958**, *109*, 741–761.
39. Mahan, G. D. *Many-Particle Physics*; Springer: New York, 1990.
40. Johnson, P. B.; Christy, R. W. Optical Constants of the Noble Metals. *Phys. Rev. B* **1972**, *6*, 4370–4379.
41. Bohren, C. F.; Huffman, D. R. *Absorption and Scattering of Light by Small Particles*; Wiley-VCH: Weinheim, Germany, 2004.